

## The Effect of Sea Surface Temperature Fronts on Atmospheric Frontogenesis

MICHAEL J. REEDER,<sup>a,b</sup> THOMAS SPENGLER,<sup>c</sup> AND CLEMENS SPENSBERGER<sup>c</sup>

<sup>a</sup> *School of Earth, Atmosphere and Environment, Monash University, Clayton, Victoria, Australia*

<sup>b</sup> *Centre of Excellence for Climate Extremes, Monash University, Clayton, Victoria, Australia*

<sup>c</sup> *Geophysical Institute, University of Bergen, and Bjerknes Centre for Climate Research, Bergen, Norway*

(Manuscript received 21 April 2020, in final form 3 March 2021)

**ABSTRACT:** It is thought that the sensible heat fluxes associated with sea surface temperature (SST) fronts can affect the genesis and evolution of atmospheric fronts. An analytic model is developed and used to explore this idea. The model predictions are compared with climatologies of atmospheric fronts over the North Atlantic Ocean identified in reanalyses. The climatologies are divided into times when fronts are detected at a point and times when they are not, and compared with model results with and without fronts in their initial conditions. In airstreams with fronts, both the climatologies and model show that adiabatic frontogenesis is much more important than diabatic frontogenesis. They also show that there is weak diabatic frontogenesis associated with differential sensible heating over the SST front and frontolysis either side of it. Because of the upstream and downstream frontolysis, the SST front has relatively little *net* effect on atmospheric fronts in the model. This result holds true as the width and strength of the SST front changes. In airstreams initially without fronts, a combination of adiabatic and diabatic frontogenesis is important for the local genesis of atmospheric fronts over the SST front. The model shows sustained frontogenesis only when the deformation is sufficiently strong or when the translation speed is low, as advection otherwise weakens the potential temperature gradient. This strong localized diabatic frontogenesis, which is amplified by adiabatic frontogenesis, can result in a front, which is consistent with atmospheric fronts in the region being most frequently located along the SST front.

**KEYWORDS:** North Atlantic Ocean; Frontogenesis/frontolysis; Fronts; Atmosphere-ocean interaction; Diabatic heating; Synoptic-scale processes


### 1. Introduction

Western boundary currents are pronounced features of the near surface midlatitude ocean circulation, the most prominent examples being the Gulf Stream, the Kuroshio, and the Agulhas Current. Strong sea surface temperature (SST) gradients, known as SST fronts, lie on the poleward flanks of the western boundary currents. In the time mean, these western boundary currents are marked by concentrated bands on convergence, high rates of precipitation (e.g., Minobe et al. 2008), and intense surface sensible and latent heat fluxes (e.g., Kelly et al. 2010; Ogawa and Spengler 2019). Consequently, western boundary currents play a part in shaping the general circulation (e.g., Robinson 2000; Minobe et al. 2010), including the storm tracks that are found along or immediately downstream (e.g., Chang et al. 2002; Nakamura et al. 2004).

Strong SST fronts are thought to affect the development of extratropical cyclones in two ways. First, the time-mean SST gradients may be imprinted on the overlying atmosphere through surface sensible and latent heating, producing regions of baroclinicity on which extratropical cyclones can develop or intensify (e.g., Hoskins and Valdes 1990; Nakamura et al. 2008; Hotta and Nakamura 2011; Papritz and Spengler 2015; Sasaki

and Yamada 2018; Small et al. 2019). Second, individual extratropical cyclones, including their associated vertical motion and precipitation, may be modified locally by the sensible and latent heat fluxes associated with an SST front (e.g., Jacobs et al. 2008; O'Neill et al. 2017; Sheldon et al. 2017; Vanni re et al. 2017; Parfitt and Seo 2018; Sasaki and Yamada 2018; de Vries et al. 2019; Masunaga et al. 2020b,a; Parfitt and Kwon 2020). Sharp SST gradients may be especially important for the most severe extratropical cyclones as a number of studies have identified a connection to their rapid deepening (e.g., Sanders and Gyakum 1980; Gyakum et al. 1989; Yoshiike and Kawamura 2009). However, recent studies have shown that SST fronts in the Gulf Stream and Kuroshio region play only a minor role in intensifying cyclones (Tsopouridis et al. 2021a,b). These findings have been supported by idealized numerical simulations, in which the SST gradient was either smoothed or shifted with respect to the cyclone propagation (Tsopouridis et al. 2020; Bui and Spengler 2021). All these studies have pointed to the more dominant role of the absolute SST in cyclone development compared with the SST gradient along SST fronts.

The theory of adiabatic and inviscid atmospheric frontogenesis rests on the pioneering work of Sawyer (1956), Eliassen (1959, 1962), Stone (1966), Williams and Plotkin (1968), and Hoskins and Bretherton (1972). These studies showed that

 Denotes content that is immediately available upon publication as open access.

Corresponding author: Michael Reeder, michael.reeder@monash.edu

DOI: 10.1175/JAS-D-20-0118.1



fronts form through deformation, which advects fluid parcels relative to each other, producing strong gradients in temperature and velocity. Extratropical cyclones generally provide the fields of deformation central to frontogenesis. Like the extratropical cyclones in which they form, atmospheric fronts may also be modified locally by the sensible and latent heat fluxes associated with the SST front. However, there has been little research to date on how these fluxes affect frontogenesis, and for this reason, it is the focus of the present study.

Some recent work on the topic is that of Parfitt et al. (2016, 2017a), who investigated the direct effect of the Gulf Stream SST front on atmospheric fronts in reanalyses and a general circulation model. They concluded that, when the SST front is weakened through smoothing or changes in the ocean resolution, the number of fronts in the Gulf Stream region and the associated precipitation decreases significantly. Parfitt et al. (2016) argued that if the temperature gradients of the SST front and atmospheric front have the same sign, and if the SST gradient is sufficiently large, then differential sensible heating will strengthen the atmospheric front as it crosses the SST front. Conversely, when the temperature gradients have the opposite sign, differential sensible heating will weaken the atmospheric front as it crosses the SST front. However, Masunaga et al. (2020b,a) have shown recently that in the Gulf Stream, Kuroshio, and Agulhas Current region, diabatic heating most strongly affects weak and quasi-stationary fronts, making the general applicability of the arguments of Parfitt et al. (2016, 2017a) to the more common developing fronts associated with cyclones unclear. Moreover, the arguments of Parfitt et al. (2016, 2017a) focus on diabatic frontogenesis associated with differential sensible heating across the SST front and do not address the adiabatic frontogenetic effect of deformation.

The aims of the present work are to examine the effect of SST fronts on atmospheric fronts, and to quantify the relative importance of adiabatic and diabatic effects on the local formation and evolution of atmospheric fronts near an SST front. To achieve these aims, a highly idealized analytic model is developed and used to explore the dynamics of adiabatic and diabatic frontogenesis, and the model predictions are compared with atmospheric fronts over the North Atlantic Ocean identified in the European Centre for Medium-Range Weather Forecasts (ECMWF) interim reanalysis (ERA-Interim; Dee et al. 2011).

## 2. Climatologies of fronts and frontogenesis in the North Atlantic

This section discusses climatologies of fronts and frontogenesis in the North Atlantic based on ERA-Interim. Theory is developed in section 3 to explain the dynamical processes shaping these climatologies.

### a. Frontogenesis function

The connection between the observations and the theory will be established through the frontogenesis function  $D|\nabla\theta|/Dt$

(Petterssen 1936), where  $\theta$  is the potential temperature and  $\nabla$  is the horizontal gradient operator. It is therefore useful to briefly summarize the relevant aspects of the frontogenesis function.

Expressed in terms of potential temperature, the first law of thermodynamics is

$$\frac{D\theta}{Dt} = \dot{\theta}, \quad (1)$$

where  $\dot{\theta}$  is the diabatic heating rate. Assuming horizontal motion only, the frontogenesis function can be written

$$\frac{D|\nabla\theta|}{Dt} = F_{\text{ad}} + F_{\text{di}}, \quad (2)$$

where  $F_{\text{ad}} = (1/2)|\nabla\theta|[E\cos(2\beta) - D]$  is the *adiabatic frontogenesis* and  $F_{\text{di}} = \mathbf{n} \cdot \nabla\dot{\theta}$  is the gradient of the diabatic heating rate normal to the isentropes or *diabatic frontogenesis* for short. Here  $\mathbf{n} = \nabla\theta/|\nabla\theta|$  is the unit vector normal to the isentropes pointing toward potentially warmer air;  $D = \nabla \cdot \mathbf{u}$  is the horizontal divergence with  $\mathbf{u}$  the horizontal component of the wind;  $E = (E_{\text{st}}^2 + E_{\text{sh}}^2)^{1/2}$  is the total deformation with  $E_{\text{st}} = \partial u/\partial x - \partial v/\partial y$  and  $E_{\text{sh}} = \partial v/\partial x + \partial u/\partial y$  the stretching and shearing deformation, respectively;  $x$  and  $y$  are horizontal rectangular cartesian coordinates; and  $\beta$  is the local angle between the axis of dilatation (the axis along which the stretching of a fluid element is most rapid; for example, see Saucier 1955) and the isentropes.

When interpreting the frontogenesis function it is important to bear in mind that  $F_{\text{ad}}$  depends nonlinearly on  $F_{\text{di}}$ , as  $F_{\text{ad}}$  is proportional to the magnitude of the horizontal potential temperature gradient. Consequently, it is not enough to examine  $F_{\text{di}}$  in isolation from  $F_{\text{ad}}$  because, if a front is strengthened (or weakened) at some instant by differential heating, the change will be amplified through  $F_{\text{ad}}$ . These ideas will be made more concrete with the aid of the theory developed in section 3.

### b. Climatology of fronts

The climatologies use ERA-Interim for winter (December, January, and February) in the years 1979–2016 with a time interval of 6 h. Although the native grid for these data is T255 (approximately  $0.7^\circ$ ), they are, for this study, interpolated to a grid with spacing  $0.5^\circ \times 0.5^\circ$ .

Following Spensberger and Sprenger (2018), a frontal volume is a region in space wherein the magnitude of the equivalent potential temperature gradient  $|\nabla\theta_e|$  exceeds  $4.5 \text{ K} (100 \text{ km})^{-1}$ . This method will be called the Spensberger–Sprenger method, and the sensitivity of the results to the frontal detection method is assessed later in the section. Frontal volumes in the North Atlantic are calculated using the Spensberger–Sprenger method, with all frontal volumes smaller than  $75\,000 \text{ km}^2 \times 250 \text{ hPa}$  neglected. As this study focuses on the evolution of the near-surface temperature field, fronts are defined by the intersection of a frontal volume with the 925 hPa isobaric surface. Note that although fronts are defined here by gradients in the equivalent potential temperature, the following calculations of the frontogenesis are based on the potential temperature. As air masses over the ocean are

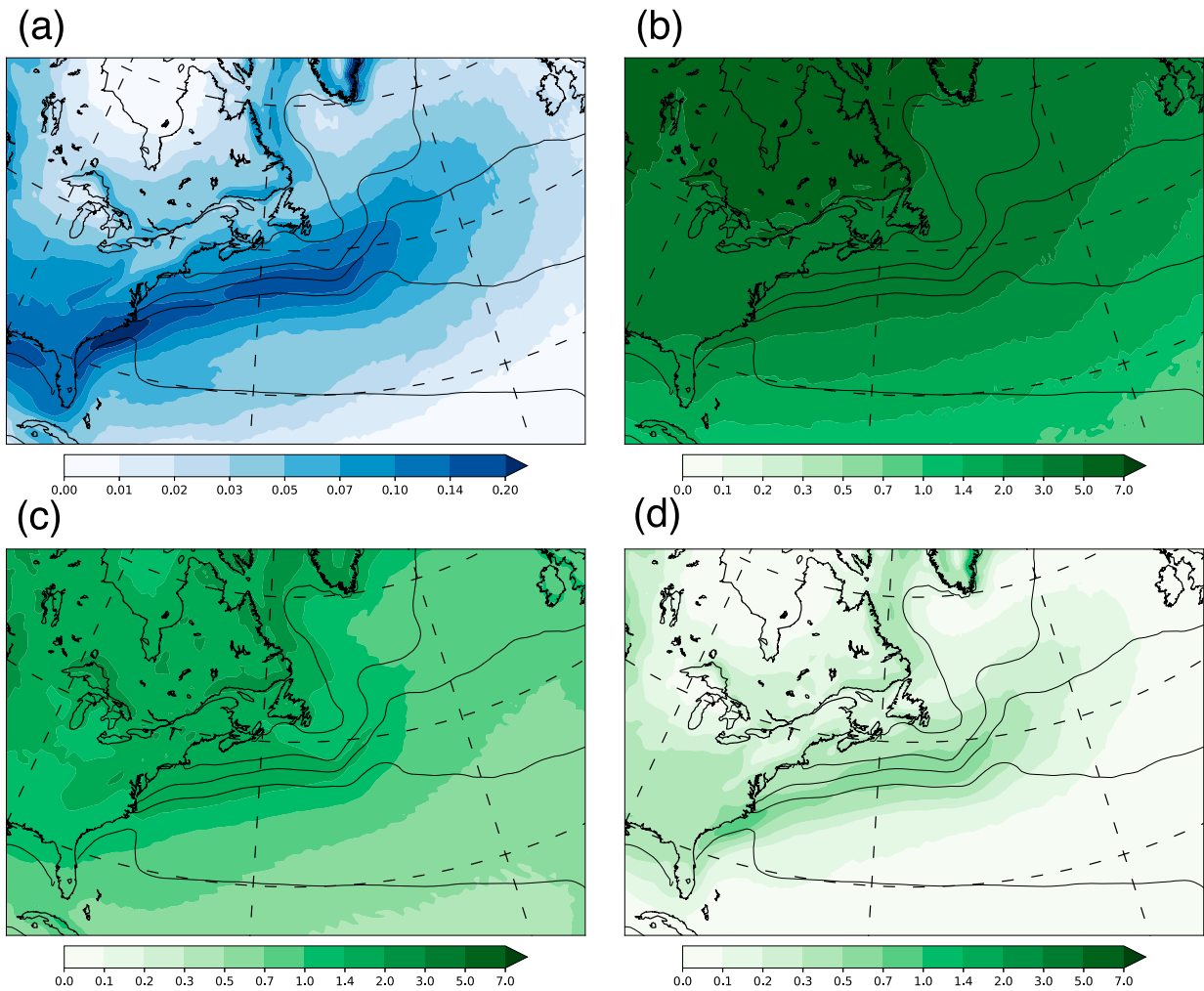


FIG. 1. (a) Frequency of occurrence of fronts  $m/M$ . (b) Conditional mean potential temperature gradient at 950 hPa when a front is detected  $\overline{|\nabla\theta|}^{\text{fr}}$ . Also shown are contributions to the climatological mean potential temperature gradient at 950 hPa (c) when a front is not detected  $\overline{|\nabla\theta|}^{\text{no}}$  and (d) when a front is detected  $\overline{|\nabla\theta|}^{\text{fr}}$ . The sum of (c) and (d) is the climatological mean potential temperature gradient at 950 hPa. Units for (b)–(d) are  $\text{K} (100 \text{ km})^{-1}$ . Note that the color scale in each panel is nonlinear. Black contours in all panels are SST isotherms with a contour interval of 5 K.

generally relatively warm and moist, the potential temperature gradients associated with fronts in the region of the SST front are generally weaker than the associated gradients in equivalent potential temperature used to define the fronts.

If  $m$  is the number of times a front is detected at a given grid point and  $M$  is the total number of analysis times in the interval 1979–2016, the frequency of occurrence is  $m/M$  (Fig. 1a; note that the color scale in this and later figures is nonlinear). Fronts are most frequent along the SST front marking the poleward side of the Gulf Stream, where they are found around 15% of the time. That the frequency maximum is so pronounced and geographically confined suggests two scenarios, which are not necessarily exclusive of one another. The first is that fronts form preferentially along the SST front, and possibly decay preferentially either side of it. The second is that there is a higher likelihood for stationary fronts along the SST front.

The mean potential temperature gradient at each grid point at 950 hPa conditioned on there being a front at that grid point is

$$\overline{|\nabla\theta|}^{\text{fr}} = \frac{1}{m} \sum_{i=1}^M |\nabla\theta|_i a_i, \tag{3}$$

where  $a_i$  is the element of a vector of length  $M$  that is either 1 or 0 depending on whether a front is detected or not. The conditional mean potential temperature gradient  $\overline{|\nabla\theta|}^{\text{fr}}$  represents the climatological strength of the fronts at a given grid point (Fig. 1b).

Fronts are climatologically strongest in the northwest over the northern parts of Canada and the Arctic and weakest in the southwest over the subtropical North Atlantic Ocean. Climatologically, the magnitude of the potential temperature gradient of fronts found in the neighborhood of the SST front is

around  $4 \text{ K (100 km)}^{-1}$ . Similar results have been reported by Berry et al. (2011) and Parfitt et al. (2017a) using different frontal detection methods. Although fronts are more numerous where the SST gradient is strongest, the potential temperature gradients are not strongest where the SST gradient is strongest (Figs. 1a,b), suggesting that strong fronts intensify relatively little as they cross the SST front.

### c. Partitioning the climatological mean potential temperature gradient

The unconditional mean potential temperature gradient at each grid point at 950 hPa is  $|\overline{\nabla\theta}| = (1/M)\sum_{i=1}^M |\nabla\theta|_i$ . It simply represents the climatological potential temperature gradient and will be referred to as the climatological mean. The climatological mean can be decomposed into contributions from times at which fronts are detected  $|\overline{\nabla\theta}|^{\text{fr}}$  and times at which they are not  $|\overline{\nabla\theta}|^{\text{no}}$  through the expression

$$|\overline{\nabla\theta}| = |\overline{\nabla\theta}|^{\text{no}} + |\overline{\nabla\theta}|^{\text{fr}} = \frac{1}{M} \sum_{i=1}^M |\nabla\theta|_i (1 - a_i) + \frac{1}{M} \sum_{i=1}^M |\nabla\theta|_i a_i. \quad (4)$$

Of course, the times without fronts also include weak baroclinic zones with equivalent potential temperature gradients weaker than  $4.5 \text{ K (100 km)}^{-1}$ . Nonetheless, both have maxima lying along the SST front, with the contribution from no fronts being about  $1.7 \text{ K (100 km)}^{-1}$  (Fig. 1d) and that from fronts being about  $0.6 \text{ K (100 km)}^{-1}$  (Fig. 1c). Thus, roughly a quarter of the climatological potential temperature gradient along the SST front can be attributed to fronts.

The contribution to the climatological potential temperature gradient from times without fronts reflects the relatively steady localized imprint on the overlying atmosphere of the coastal and ice-edge gradients, and the SST front (Fig. 1c). In contrast, the contribution to the climatological potential temperature gradient from times with fronts (Fig. 1d) appears to reflect the increased frequency of fronts in the neighborhood of the SST front (Fig. 1a) rather than a systematic increase in their intensity in the region (cf. Fig. 1b). Nonetheless, the intensity plays a part indirectly as the frequency maximum is due in part to weak baroclinic zones crossing the SST front, being strengthened locally by both diabatic and adiabatic processes, and reaching the threshold required to be identified as a front. The theory developed in the next section (section 3) will help interpret these results.

### d. The relative importance of convergence, adiabatic and diabatic frontogenesis

In ERA-Interim, the contribution from divergence to frontogenesis over the North Atlantic Ocean is nearly an order of magnitude smaller than that from deformation (see Fig. 2 and noting that the color scale is nonlinear). Consequently, as expected, the ageostrophic circulation plays a secondary role in frontogenesis compared to the geostrophic circulation. Moreover, it has been hypothesized that differential vertical mixing of the horizontal momentum is important for frontogenesis in the region of strong SST fronts (e.g., Putrasahan et al. 2013), the idea being that the differential mixing produces coherent regions of convergence in the

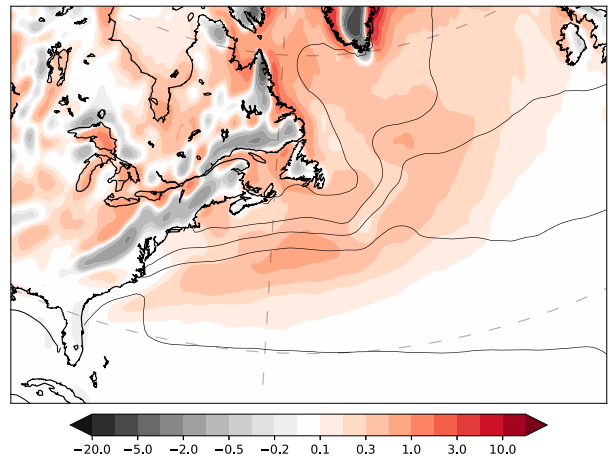


FIG. 2. Convergence frontogenesis at 950 hPa. Note that the color scale is nonlinear. Units are  $10^{-10} \text{ K (m s)}^{-1} \approx \text{K (100 km)}^{-1} (\text{day})^{-1}$ . Black contours are SST isotherms with a contour interval of 5 K.

boundary layer that strengthens the front. That the contribution from divergence to frontogenesis is small suggests differential vertical mixing may play a role, but not the primary role.

Since the divergence term is small, the adiabatic frontogenesis can be reasonably approximated as  $F_{\text{ad}} \approx (1/2)|\nabla\theta| E \cos(2\beta)$ . In this case, the relative importance of the adiabatic and diabatic frontogenesis is

$$\frac{|F_{\text{ad}}|}{|F_{\text{di}}|} = \frac{1}{2} \frac{|\nabla\theta| |E \cos(2\beta)|}{|\mathbf{n} \cdot \nabla\theta|}. \quad (5)$$

From Eq. (5), the relative importance is directly proportional to the product of the deformation and the magnitude of the potential temperature gradient, and inversely proportional to the magnitude of the differential diabatic heating across the front. The implication is that, for a fixed deformation and fixed orientation of the front, strong fronts are less affected by differential diabatic heating than airstreams with weak or non-existent temperature gradients.

Motivated by the implications of Eq. (5), the conditional and climatological means for the adiabatic and diabatic frontogenesis are calculated using expressions equivalent to Eqs. (3) and (4) (Fig. 3). The conditional mean adiabatic frontogenesis  $\overline{F_{\text{ad}}^{\text{fr}}}$  (Fig. 3a) and conditional mean diabatic frontogenesis  $\overline{F_{\text{di}}^{\text{fr}}}$  (Fig. 3b) describe the mean frontogenetic processes at a point when a front is detected at that point.

The conditional mean adiabatic frontogenesis (Fig. 3a) is almost exclusively positive, the exceptions being small regions on the western shore of Lake Superior, along the east coast orography of North America, and the eastern coast of Greenland. Thus, climatologically, the local deformation associated with each front acts to strengthen it by contracting the preexisting local potential temperature gradient. Over the ocean, the largest positive values lie in the north, the smallest values to the south and southeast, and a local maximum exceeding  $10 \times 10^{-10} \text{ K (m s)}^{-1}$  is centered on the western end of

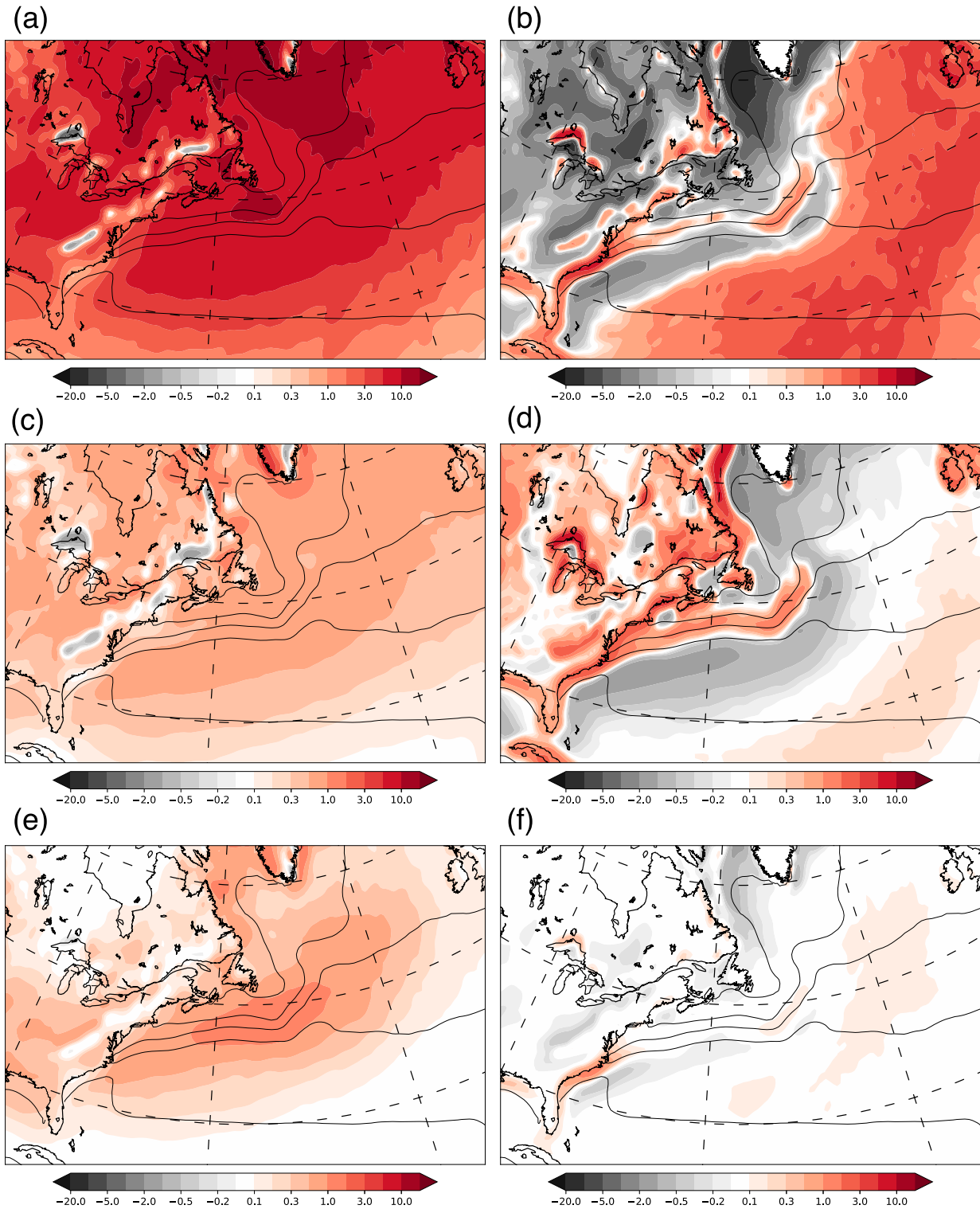


FIG. 3. (left) Adiabatic frontogenesis at 950 hPa. (right) Diabatic frontogenesis at 950 hPa. (top) Conditional mean when a front is detected: (a) Adiabatic frontogenesis  $\overline{F_{ad}^{fr}}$  and (b) diabatic frontogenesis  $\overline{F_{di}^{fr}}$ . (middle) Contributions to the climatological mean when a front is not detected: (c) adiabatic frontogenesis  $\overline{F_{ad}^{no}}$  and (d) diabatic frontogenesis  $\overline{F_{di}^{no}}$ . (bottom) Contributions to the climatological mean when a front is detected: (e) adiabatic frontogenesis  $\overline{F_{ad}^{fr}}$  and (f) diabatic frontogenesis  $\overline{F_{di}^{fr}}$ . The sum of (c) and (e) is the climatological mean frontogenesis at 950 hPa associated with deformation. The sum of (d) and (f) is the climatological mean frontogenesis at 950 hPa associated with differential heating. Note that the color scale is nonlinear. Units in all panels are  $10^{-10} \text{ K (m s)}^{-1} \approx \text{K (100 km)}^{-1} \text{ (day)}^{-1}$ . Black contours in all panels are SST isotherms with a contour interval of 5 K.

the SST front. Along the SST front, the conditional mean adiabatic frontogenesis is more than  $5 \times 10^{-10} \text{ K (m s)}^{-1}$ .

The conditional mean diabatic frontogenesis (Fig. 3b) is mostly negative in the northwestern side of the domain, which covers North America and the regions of sea ice. These regions are frontolytic because the underlying surface is relatively homogeneous, leading to a relatively positive heat flux on the cold side of the front and a relatively negative heat flux on the warm side of the front. Along the coastlines of the southern half of North America and along the SST front, the diabatic frontogenesis is also positive. There is frontogenesis in these regions, as the SST and coastal gradients mostly reinforce the atmospheric frontal gradients. Thus, climatologically, differential heating strengthens fronts when they lie over the SST front, but weakens them either side of the SST front. While not the focus of the present paper, the conditional mean diabatic frontogenesis is exclusively positive on the southern and eastern parts of the North Atlantic Ocean. This is most likely associated with isolated regions of convective heating, where diabatic heating in buoyant updrafts further enhances local temperature gradients (not shown).

Although spatially variable, typical values of the conditional mean diabatic frontogenesis near the SST front are much less than  $1 \times 10^{-10} \text{ K (m s)}^{-1}$ . Thus, in general, the conditional mean adiabatic frontogenesis near the SST front is an order of magnitude larger than its diabatic counterpart. This result is consistent with Eq. (5). Moreover, a local maximum in the adiabatic frontogenesis lies on the SST front, presumably reflecting the nonlinear connection between  $F_{\text{ad}}$  and  $F_{\text{di}}$ .

The patterns of the climatological mean adiabatic and diabatic frontogenesis from times without fronts  $\overline{F_{\text{ad}}^{\text{no}}}$  and  $\overline{F_{\text{di}}^{\text{no}}}$  (Figs. 3c,d) are broadly similar to the patterns of the conditional mean adiabatic and diabatic frontogenesis (Figs. 3a,b). The main exceptions are that the amplitudes of the climatological means are lower (Figs. 3c,d), and the climatological mean diabatic frontogenesis is positive over North America (Fig. 3d). Importantly, diabatic processes at times without fronts are generally more important than adiabatic processes. This result is consistent with Eq. (5), as the potential temperature gradient is by definition relatively small in this case.

The general patterns of the climatological mean adiabatic and diabatic frontogenesis from times with fronts  $\overline{F_{\text{ad}}^{\text{fr}}}$  and  $\overline{F_{\text{di}}^{\text{fr}}}$  (Figs. 3e,f) are similar to the equivalent fields for times without fronts (Figs. 3c,d), although the adiabatic contribution is more focused on the SST front and, of particular importance, the diabatic contribution is negligible everywhere except near the coastline of the southeastern United States. Thus, as foreshadowed by Eq. (5), virtually all of the climatological mean diabatic frontogenesis comes from times without fronts (cf. Fig. 3d with Fig. 3f). Even though atmospheric fronts only lie along the SST front around 15% of the time (Fig. 1a), they contribute the greater part of the climatological adiabatic frontogenesis in the neighborhood of the SST front (cf. Fig. 3c with Fig. 3e).

Investigating the interaction of cold fronts with the underlying Gulf Stream SST front, Parfitt et al. (2017a) calculated the cross-front gradient of the surface sensible heat flux to infer the sign of diabatic frontogenesis. Their pattern of cross-front

surface sensible heat flux gradient (their Figs. 3a,b) is comparable to the pattern of climatological mean diabatic frontogenesis found here (Fig. 3d), with frontogenesis along the SST front, strong frontolysis on the southeastern side, and weak frontolysis on the northwestern side. Similar results were found in a general circulation model by Parfitt et al. (2016). In the present study, however, most of the diabatic frontogenesis along the SST front is associated with no front conditions (cf. Fig. 3d with Fig. 3f), whereas in the presence of a front, it is mainly the adiabatic frontogenesis that contributes to the climatological frontogenesis in the region (Fig. 3e).

The key points from the analysis are (i) adiabatic frontogenesis due to deformation is the dominant mechanism for frontogenesis at fronts in the North Atlantic region, while in nonfrontal airstreams adiabatic frontogenesis is comparable to diabatic frontogenesis due to differential surface sensible heating; (ii) the direct effect of differential surface sensible heating on atmospheric fronts is weak, whereas the direct effect on nonfrontal airstreams is strong; and (iii) differential surface sensible heating also affects atmospheric fronts indirectly as the deformation amplifies the direct effect, as evidenced by the local maximum in adiabatic frontogenesis along the SST front. Taken together these results suggest that the combination of diabatic and adiabatic frontogenesis in initially nonfrontal airstreams is largely responsible for the maximum in the number of fronts detected along the SST fronts. In other words, along the SST front, diabatic frontogenesis or weaker diabatic frontolysis together with the amplification by the adiabatic frontogenesis produces equivalent potential temperature gradients that, with sufficient frontogenesis, overcome the detection threshold.

#### e. Sensitivity of the results to the detection method, frontal type, and analysis period

There is no agreed definition for a front and no standard method for their detection in observations, reanalyses, or models. For a recent review of how fronts are defined and detected see Thomas and Schultz (2019). This subsection explores the sensitivity of the results to some of the definitions, detection methods, and analysis period used here.

The climatologies of fronts and frontogenesis discussed above are based on the Spensberger–Sprengrer method using the equivalent potential temperature. The calculations are repeated now, but with the potential temperature replacing equivalent potential temperature (Fig. 4). The frequency of occurrence is greater when potential temperature is used, the maximum being slightly more than doubled, and the coastal temperature gradients are more prominent (Fig. 4a). The climatological patterns of frontogenesis, however, are very similar (cf. Figs. 4b–e with Figs. 3c–f). Perhaps the main difference is in the contribution to the climatological mean diabatic frontogenesis when a front is detected (cf. Fig. 4e with Fig. 3f). In this case, the frontolysis on either side of the SST front is stronger, and there is now frontogenesis along much of the coastline of North America.

Fronts are generally characterized by enhanced horizontal temperature gradients, cyclonic relative vorticity, and regions of convergence. The local maxima in these quantities are often

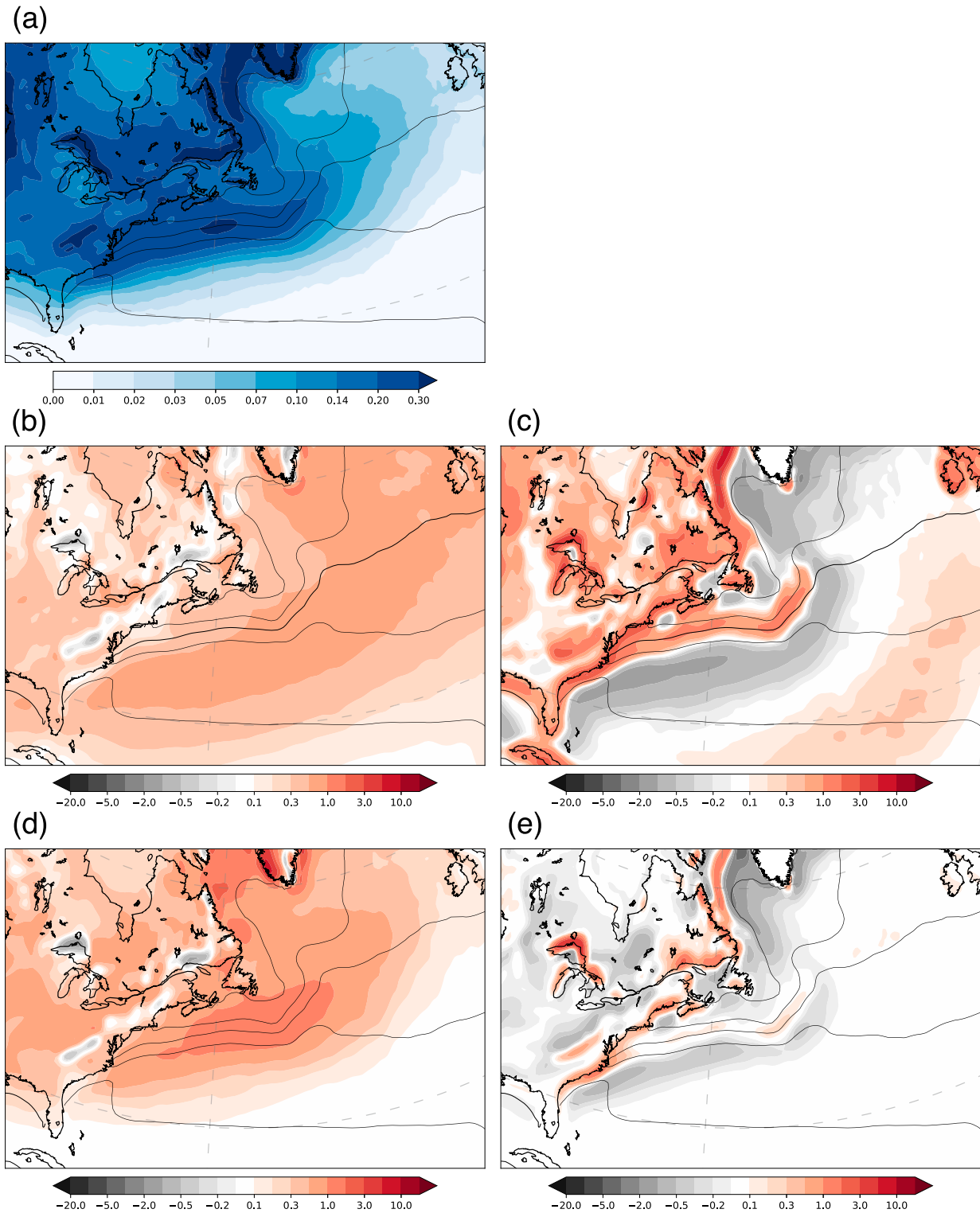


FIG. 4. Frontal detection based on potential temperature. (a) Frequency of occurrence of fronts  $m/M$ . (middle) Contributions to the climatological mean when a front is not detected: (b) adiabatic frontogenesis  $\bar{F}_{ad}^{no}$  and (c) diabatic frontogenesis  $\bar{F}_{di}^{no}$ . (bottom) Contributions to the climatological mean when a front is detected: (d) adiabatic frontogenesis  $\bar{F}_{ad}^{fr}$  and (e) diabatic frontogenesis  $\bar{F}_{di}^{fr}$ . The sum of (b) and (d) is the climatological mean frontogenesis at 950 hPa associated with deformation. The sum of (c) and (e) is the climatological mean frontogenesis at 950 hPa associated with differential heating. Note that the color scales are nonlinear. In (b)–(e) the units are  $10^{-10} \text{ K (m s)}^{-1} \approx \text{K (100 km)}^{-1} (\text{day})^{-1}$ . Black contours in all panels are SST isotherms with a contour interval of 5 K.

widely separated but, at least in theoretical models of frontogenesis, coalesce as a frontal discontinuity forms (Smith and Reeder 1988). Consequently, only in the strongest fronts are these three maxima collocated. Because fronts are marked by enhanced horizontal temperature gradients and cyclonic relative vorticity, Solman and Orlanski (2010) defined a frontal activity index as the product of the relative vorticity and the horizontal temperature gradient. Later, Parfitt et al. (2017b) normalized the frontal activity parameter and defined a front by those points where it exceeded one. This detection method is called here the Parfitt–Czaja–Seo method. In this method, the relative vorticity is normalized by the local value of the planetary vorticity and the horizontal temperature gradient by  $0.45 \text{ K (100 km)}^{-1}$ , which is one tenth of the threshold used in the Spensberger–Sprengrer method. Even though the threshold horizontal temperature gradient is low and the relative vorticity at a front will almost always be larger than the planetary vorticity, the Parfitt–Czaja–Seo method does not identify much weaker baroclinic zones as fronts than the Spensberger–Sprengrer method. This is because, as noted above, the maxima in the temperature gradient and relative vorticity are usually separated.

The calculations described in the preceding sections are repeated using the Parfitt–Czaja–Seo method (Fig. 5). The frequency of occurrence is much the same as that using the Spensberger–Sprengrer method with equivalent potential temperature, although the fronts are much less localized to the SST front (cf. Fig. 5a with Fig. 1a). The fronts are most frequent over the ocean on the cold side of the SST front, while on the warm side they become less frequent toward the south and east. The climatological patterns of frontogenesis are very similar to those obtained with the Spensberger–Sprengrer method (cf. Figs. 5b–e with Figs. 3c–f). The main difference in the pattern obtained from the Parfitt–Czaja–Seo method is in the contribution to the climatological mean diabatic frontogenesis when a front is detected, which is frontolytic everywhere except for some sections of the coastline, including the Great Lakes.

In one of the landmark papers in the theory of fronts, Sawyer (1956) argued that fronts are not static boundaries separating two contrasting air mass, but instead are the sites of active frontogenesis by deformation. In a similar vein, Thomas and Schultz (2019) suggest that the (adiabatic) Petterssen frontogenesis function can be a useful way to locate fronts in gridded dataset. From this perspective  $F_{ad}$  is another frontal detection method. The three detection methods examined here produce remarkably similar dynamical pictures as revealed in the patterns of adiabatic frontogenesis (cf. the sum of Figs. 3c,e with the sum of Figs. 4b,d, and the sum of Figs. 5b,d). In each case the adiabatic frontogenesis is focused on the SST front as it amplifies the effects of differential heating.

The results reported above do not depend substantially on the type of front. The fronts detected using the Spensberger–Sprengrer method with equivalent potential temperature are subdivided into frontal types according to the magnitude and sign of the component of the wind in the direction of the equivalent potential temperature gradient,  $c_f = \mathbf{u} \cdot \nabla\theta_e/|\nabla\theta_e|$ . Warm fronts are defined by  $c_f \leq -1.5 \text{ m s}^{-1}$ , stationary fronts by  $-1.5 < c_f < 1.5 \text{ m s}^{-1}$ , and cold fronts by  $c_f \geq 1.5 \text{ m s}^{-1}$ . Like

that for all fronts (Fig. 3a), the conditional mean adiabatic frontogenesis for cold fronts and warm fronts is almost everywhere positive (Figs. 6a,b). The main differences are that maxima for the cold fronts and warm fronts lie on the warm and cold sides of the SST gradient, respectively, which is consistent with the common relative position of warm and cold fronts in extratropical cyclones. The conditional mean diabatic frontogenesis for cold fronts (Fig. 6c) closely matches that for all fronts (Fig. 3b), whereas the frontolysis on the warm side of the SST front is much weaker for warm fronts (Fig. 3d) than cold fronts. The climatological mean adiabatic and diabatic frontogenesis from times with fronts (Figs. 3e,f) are similar to their counterparts for cold fronts and warm fronts (Figs. 6e–h). The results for stationary fronts are similar, but make a much weaker contribution (not shown).

As noted by Parfitt et al. (2017a), the resolution of the SST used in ERA-Interim changed from  $1^\circ \times 1^\circ$  to  $0.5^\circ \times 0.5^\circ$  in 2001 and then to  $0.05^\circ \times 0.05^\circ$  in 2009. For this reason, the robustness of the results to changes in the SST resolution is tested by repeating the calculations for the periods 1979–2001 and 2002–16 separately. As there was little difference in the results for the two periods, the whole ERA-Interim dataset has been used in all the calculations reported here.

### 3. One-dimensional model of frontogenesis

To explain theoretically the climatologies reported in section 2, the advection of an airstream across an SST front is investigated in a simple geometrical configuration. Motivated by the climatologies, two cases are explored. In the first case, there is no atmospheric potential temperature gradient at the initial time, whereas in the second case the initial condition includes a weak potential temperature gradient. They will be called the *no front* and *front* cases, respectively. The role of deformation will be explored in both cases. The model is deliberately minimalist and, among other things, neglects all boundary layer processes apart from surface sensible heating and all moist processes.

#### a. Model formulation and solution

Assume a rectangular cartesian coordinate system  $(x, y)$  and a wind field defined by  $\mathbf{u} = (u, v) = \alpha(x, -y)$ . The wind field is irrotational, nondivergent, and has constant deformation  $E = 2\alpha$  with the axis of dilatation parallel to the  $x$  axis. Such a wind field has hyperbolic streamlines defined by  $\psi = -\alpha xy$  and has been used in numerous studies of frontogenesis (e.g., Bergeron 1928; Petterssen 1936; Stone 1966; Williams 1967; Hoskins and Bretherton 1972; Keyser et al. 1988; among many others).

The wind advects a near-surface potential temperature field  $\theta(y, t)$ , which has the isentropes aligned parallel to the axis of dilatation for simplicity. The surface fluxes are assumed to be proportional to the difference between the potential temperature and the SST field  $T_S(y, t)$ . The evolution of the potential temperature is governed by Eq. (1), reexpressed as

$$\frac{\partial\theta}{\partial t} - \alpha y \frac{\partial\theta}{\partial y} = \dot{\theta}, \quad (6)$$



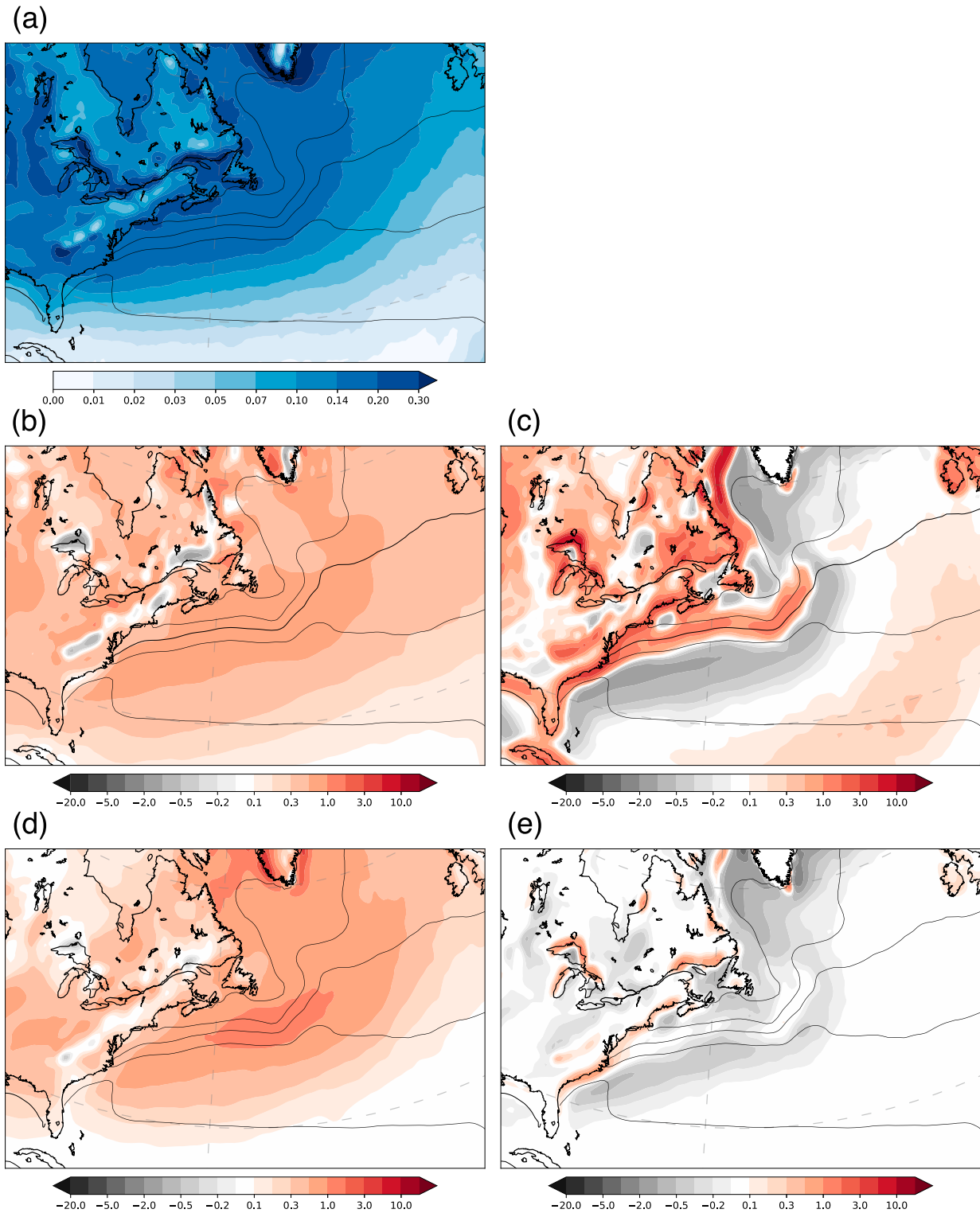


FIG. 5. Frontal detection based on the Parfitt–Czaja–Seo method. (a) Frequency of occurrence of fronts  $m/M$ . (middle) Contributions to the climatological mean when a front is not detected: (b) adiabatic frontogenesis  $\overline{F_{ad}^{no}}$  and (c) diabatic frontogenesis  $\overline{F_{di}^{no}}$ . (bottom) Contributions to the climatological mean when a front is detected: (d) adiabatic frontogenesis  $\overline{F_{ad}^{fr}}$  and (e) diabatic frontogenesis  $\overline{F_{di}^{fr}}$ . The sum of (b) and (d) is the climatological mean frontogenesis at 950 hPa associated with differential heating. The sum of (c) and (e) is the climatological mean frontogenesis at 950 hPa associated with deformation. Note that the color scales are nonlinear. In (b)–(e) the units are  $10^{-10} \text{ K (m s)}^{-1} \approx \text{K (100 km)}^{-1} (\text{day})^{-1}$ . Black contours in all panels are SST isotherms with a contour interval of 5 K.

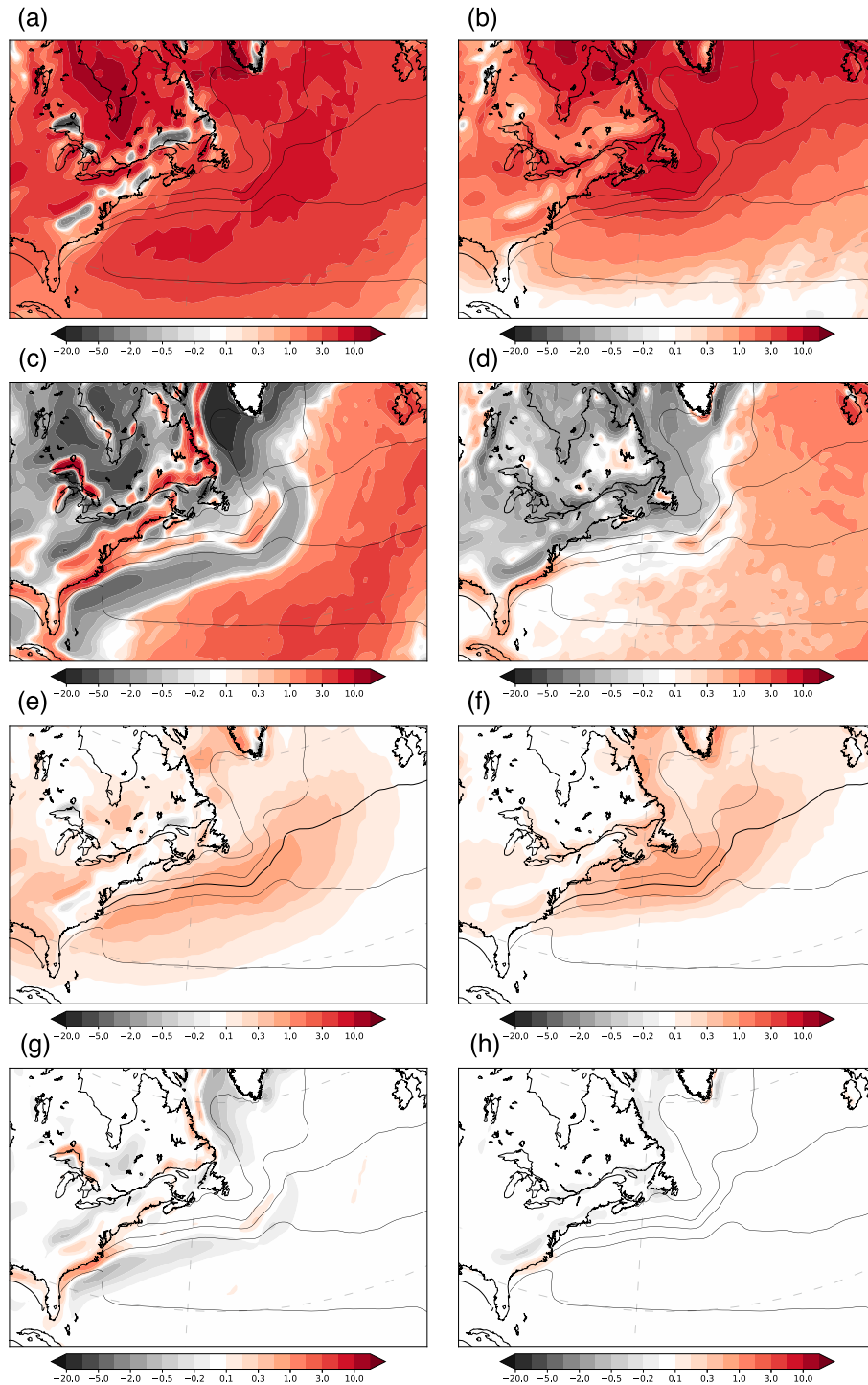


FIG. 6. (top) Conditional mean adiabatic frontogenesis at 950 hPa when a front is detected  $\overline{F_{ad}^{fr}}$ : (a) cold and (b) warm fronts. (second row) Conditional mean diabatic frontogenesis at 950 hPa when a front is detected  $\overline{F_{di}^{no}}$ : (c) cold and (d) warm fronts. (third row) Contributions to the climatological mean adiabatic frontogenesis at 950 hPa when a front is detected  $\overline{F_{ad}^{fr}}$ : (e) cold and (f) warm fronts. (bottom) Contributions to the climatological mean diabatic frontogenesis at 950 hPa when a front is detected  $\overline{F_{di}^{fr}}$ : (g) cold and (h) warm fronts. Note that in all panels the color scale is nonlinear with units  $10^{-10} \text{ K (m s)}^{-1} \approx \text{K (100 km)}^{-1} (\text{day})^{-1}$ . Black contours in all panels are SST isotherms with a contour interval of 5 K.

where  $\hat{\theta} = \mu(T_S - \theta)$  and  $\mu$  is the strength of the coupling. Physically, the right-hand side of Eq. (6) represents the surface sensible heating of the atmosphere by the ocean, which is positive when  $T_S > \theta$ . From Eq. (6), the adiabatic and diabatic parts of the frontogenesis function reduce to  $F_{ad} = \alpha|\partial\theta/\partial y|$  and  $F_{di} = \mu\partial(T_S - \theta)/\partial y$ , respectively.

For the special case  $\mu = 0$ , there is no coupling between the sea surface and the atmosphere and the solution is  $\theta(y, t) = \theta_i(ye^{\alpha t})$ , where  $y = y_i e^{-\alpha t}$  defines the characteristic curves,  $\theta(y, 0) = \theta_i(y_i)$  is the initial potential temperature field, and  $y_i$  is the initial value of  $y$ . As the characteristics are also parcel trajectories, this solution physically represents the rearrangement of the initial potential temperature field by the wind field. If  $\mu$  is a nonzero constant, the solution to Eq. (6) is

$$\theta(y, t) = \theta_i(ye^{\alpha t})e^{-\mu t} + \mu e^{-\mu t} \int_0^t e^{\mu\tau} T_S(y, \tau) d\tau. \quad (7)$$

The value for  $\mu$  is motivated as follows. Taking  $T_S - \theta = 10$  K and  $\mu = 1/(37 \text{ h}) = 7.5 \times 10^{-6} \text{ s}^{-1}$  gives a heating rate of  $6.4 \text{ K day}^{-1}$ , which is consistent with the climatology in Minobe et al. (2010). Assuming a mixed layer depth of 300 m, this heating rate is consistent with a surface sensible heating of  $100 \text{ W m}^{-2}$ , which is also consistent with climatology.

The SST distribution features a front and is defined by

$$T_S(y, t) = T_0 - \frac{\Delta T}{2} \tanh\left[\frac{(y - y_0) - ct}{h}\right], \quad (8)$$

where  $T_0 = 280 \text{ K}$ ,  $\Delta T = 15 \text{ K}$ ,  $c = 10 \text{ m s}^{-1}$ , and  $h = 200 \text{ km}$  are constants representing the mean SST, the temperature difference across the SST front, the translation speed of the SST front, and a measure of the width of the SST front, respectively. These constants, and the others needed for the model, are typical values derived from ERA-Interim for Northern Hemisphere winter. The position of the SST front at the initial time is  $y_0 = -86.4c \text{ km}$  and is defined so that the SST front reaches  $y = 0$  at 24 h.

Although Eq. (8) represents a straight SST front translating with speed  $c$ , the configuration defined by Eqs. (7) and (8) can be thought of as an atmospheric wind field and temperature distribution advancing at speed  $-c$  with the SST field stationary. Hence, a positive value of  $c$  corresponds to an SST front moving in the positive  $y$  direction beneath a stationary atmosphere, or a stationary SST front with an atmosphere moving in the negative  $y$  direction. The latter perspective is adopted in the following.

To complete the solution, the potential temperature at the initial time is defined by

$$\theta_i(y) = \theta_0 - \frac{\Delta\theta}{2} \tanh\left(\frac{y}{d}\right), \quad (9)$$

where  $\theta_0 = 280 \text{ K}$  and  $d = 500 \text{ km}$  are constants representing the mean potential temperature and a measure of the width of the initial potential temperature gradient, respectively. Physically, Eq. (9) represents a straight baroclinic zone aligned with the  $x$  axis and  $\Delta\theta$  represents the potential temperature difference across the baroclinic zone. To model a no front case,  $\Delta\theta$  is set to zero, whereas to model a front case,  $\Delta\theta$  is taken to be  $20 \text{ K}$ . For the constants chosen, the maximum initial potential temperature gradient is  $2 \times 10^{-5} \text{ K m}^{-1}$ .

Substituting Eqs. (8) and (9) into Eq. (7) gives

$$\begin{aligned} \theta(y, t) = & T_0 + (\theta_0 - T_0)e^{-\mu t} - \frac{\Delta\theta}{2} e^{-\mu t} \tanh\left(\frac{ye^{\alpha t}}{d}\right) \\ & + \frac{\Delta T}{2} \mu e^{-\mu t} \int_0^t e^{\mu\tau} \tanh\left[\frac{ye^{-\alpha(\tau-t)} - c\tau}{h}\right] d\tau. \end{aligned} \quad (10)$$

### b. Model results

In the no front case without deformation ( $\Delta\theta = 0 \text{ K}$ ,  $\alpha = 0 \text{ s}^{-1}$ ), the potential temperature is initially uniform. This airstream is directed from the cold side of the SST front, which is  $272.5 \text{ K}$ , to the warm side, which is  $287.5 \text{ K}$ . The surface sensible heating relaxes the potential temperature toward the SST. Thus, at 50 h into the integration, there is a geographically fixed diabatic frontogenesis centered on the SST front and a region of diabatic frontolysis stretching downstream toward more negative  $y$  (Fig. 7a). This downstream region is frontolytic because the potential temperature relaxes back toward the uniform SST. Consequently, the potential temperature gradient is largest near the center of the SST front and becomes progressively weaker downstream. As there is no deformation, there is no adiabatic frontogenesis. However, when deformation is added to the no front case, the leading edge of the potential temperature gradient is sharpened, and the maximum is found downstream of the SST (Fig. 7b). On the downstream side of the SST front, the net frontogenesis is negative, although the adiabatic frontogenesis compensates the diabatic frontogenesis to a large degree.

These no front solutions are consistent with the ERA-Interim based climatology (Figs. 3c,d). In the climatology, the magnitude of the maximum potential temperature gradient and the maximum diabatic frontogenesis are around  $1 \times 10^{-5} \text{ K m}^{-1}$  and  $2 \times 10^{-10} \text{ K (m s)}^{-1}$ , respectively; a region of adiabatic frontogenesis lies over and on the warm side of the SST front; and the diabatic frontogenesis is positive over the SST front and negative on the warm side.

For the front case with deformation ( $\alpha = 1 \times 10^{-5} \text{ s}^{-1}$ ), the potential temperature front lies initially on the cold side of the SST front (Fig. 8a). The adiabatic frontogenesis, through deformation, and the diabatic frontolysis, through the relaxation to the underlying SST, largely cancel, leaving a small region of residual frontogenesis in the neighborhood of the front. Over the SST front, both the adiabatic and diabatic processes are frontogenetic.

At 20 h, the potential temperature front is almost coincident with the SST front (Fig. 8b). The diabatic processes produce frontogenesis near the center of the SST front with frontolysis on either side. This pattern and its amplitude compares favorably with climatology (Fig. 3b). Likewise, the amplitude of the adiabatic frontogenesis is similar to climatology (Fig. 3a). At this time, the potential temperature gradient is  $3 \times 10^{-5} \text{ K m}^{-1}$ , which is similar to that observed (Fig. 1b).

At 50 h, the potential temperature front lies around 1000 km to the warm side of the SST front (Fig. 8c). The adiabatic and diabatic frontogenesis largely cancel near the potential temperature front resulting in weak frontogenesis. Over the

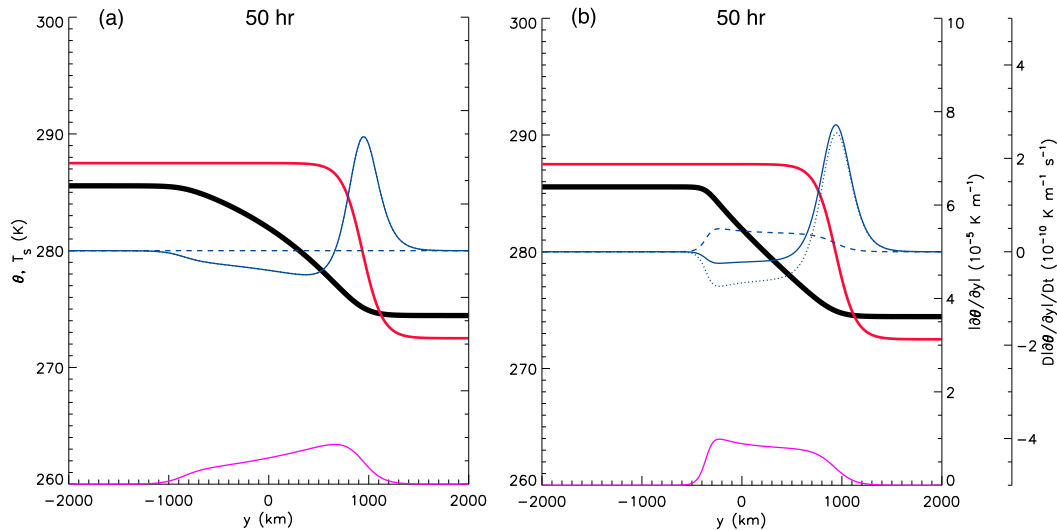


FIG. 7. One-dimensional model for the no front case at 50 h with  $\Delta\theta = 0$  K and  $c = 10 \text{ m s}^{-1}$ . (a)  $\alpha = 0 \text{ s}^{-1}$ , corresponding to curve vi in Fig. 9a. (b) Control solution with  $\alpha = 0.5 \times 10^{-5} \text{ s}^{-1}$ , corresponding to curve i in Fig. 9a. Potential temperature  $\theta$  (black), sea surface temperature  $T_s$  (red), magnitude of the potential temperature gradient  $|\partial\theta/\partial y|$  (magenta), and frontogenesis  $D|\partial\theta/\partial y|/Dt$  (blue). Adiabatic frontogenesis  $F_{ad} = \alpha|\partial\theta/\partial y|^{-1}\partial\theta/\partial y$  (dashed blue lines) and diabatic frontogenesis  $F_{di} = \mu|\partial\theta/\partial y|^{-1}(\partial\theta/\partial y - \partial T_s/\partial y)$  (dotted blue lines).

SST front, the adiabatic and diabatic frontogenesis reinforce each other. However, the potential temperature gradient over the SST front remains weak as it is continuously advected downstream.

### c. Sensitivity to the chosen constants

Having established the spatial patterns of potential temperature gradient and frontogenesis, the time evolution of the solutions and their sensitivity to the choice of constants is now explored.

#### 1) NO FRONT

The first solution discussed in the no front case is called the *no front control solution* (Fig. 9a, line i). The constants chosen for the control solution are  $\alpha = 0.5 \times 10^{-5} \text{ s}^{-1}$ ,  $c = 10 \text{ m s}^{-1}$ , and  $h = 200 \text{ km}$ . These choices for the deformation, translation speed, and width of the SST front are motivated by the climatologies on times without fronts, and are referred to as the *standard values*. Table 1 lists the constants chosen for each of the solutions discussed.

For the control simulation, the maximum potential temperature gradient  $[\max(|\partial\theta/\partial y|)]$  strengthens for the first day and a half as the SST front imprints itself on the overlying atmosphere (Fig. 9a). After this, however, the maximum potential temperature gradient weakens slowly as the air is advected downwind over relatively uniform SSTs.

In contrast, when there is no deformation and no translation, the maximum potential temperature gradient increases uniformly (Fig. 9a, line ii). If the deformation is retained while the translation is set to zero, the maximum potential temperature gradient strengthens even more rapidly as the developing gradient remains collocated with the SST gradient (Fig. 9a, line iii). In contrast, if the deformation is retained and the translation

doubled, the maximum potential temperature gradient strengthens initially, but thereafter slowly weakens (Fig. 9a, line iv).

This result underscores that the frontogenetic effect of the SST front, which is geographically fixed, depends on how long air parcels remain near it. The rate of frontogenesis depends on the background deformation, even when there is no potential temperature gradient in the initial conditions, because it acts on the potential temperature gradient produced by the SST front (Fig. 9a, lines v and vi).

Decreasing the width of the SST front increases the strength of the SST front and initially increases the rate of frontogenesis (Fig. 9a, line vii). This effect is transient, however, with the maximum potential temperature gradient weakening rapidly after about 18 h (Fig. 9a, line vii). Although perhaps counterintuitive, by 50 h, the maximum potential temperature gradient in the solution with double the SST gradient (Fig. 9a, line vii) is not much different from that in which the SST gradient is halved (Fig. 9a, line viii). Although frontogenesis is enhanced by the stronger SST front, the effect is more transient as the SST front is narrower and thus the time available for the interaction shorter.

#### 2) FRONT

The transience of the diabatic frontogenesis is even more apparent in the front case. The solution with a front using the standard values is called the *front control solution* (Fig. 9a, line i). In this solution, the front weakens initially as it approaches the SST front. It then strengthens as it crosses the SST front and weakens again as it moves downstream, leaving the maximum potential temperature gradient not much different from its initial value as the atmospheric potential temperature relaxes to SST temperature.

Doubling the translation speed leaves the front weaker after the interaction with the SST front (Fig. 9b, line iv) as the time

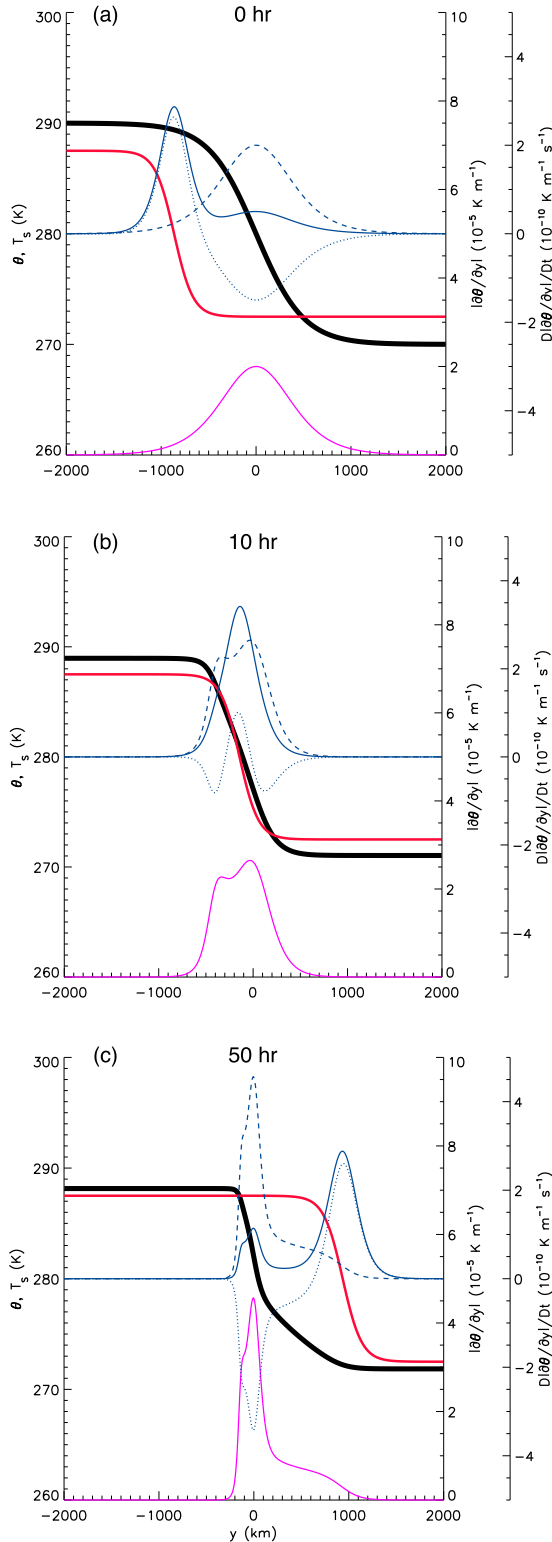


FIG. 8. One-dimensional model for the front case. Control solution with  $\Delta\theta = 20\text{ K}$ ,  $\alpha = 0.5 \times 10^{-5}\text{ s}^{-1}$ , and  $c = 10\text{ m s}^{-1}$ , corresponding to curve i in Fig. 9b. (a) 0, (b) 10, and (c) 50 h. Potential temperature  $\theta$  (black), sea surface temperature  $T_S$  (red), magnitude of the potential temperature gradient  $|\partial\theta/\partial y|$

where the front coincides with the SST front is half as long. In contrast, if the front is stationary (Fig. 9b, line iii), the adiabatic and diabatic frontogenesis both strengthen the front in situ. Setting both the deformation and the translation to zero (Fig. 9b, line ii) captures the effect of diabatic frontogenesis alone on a front that remains stationary on the SST front. In this solution, the strength of the front increases at a relatively uniform rate.

When the deformation is doubled, the front strengthens monotonically, with the highest rates of frontogenesis as it crosses the SST front (Fig. 9b, line v). Likewise, when the deformation is halved, the maximum potential temperature gradient weakens upstream of the SST front, strengthens over the SST front, and weakens again downstream of the SST front (Fig. 9b, line vi). Halving the width of the SST front weakens the interaction with the front (Fig. 9b, line viii), whereas doubling the width strengthens the interaction (Fig. 9b, line vii). Nonetheless, there is little net change in the strength of the front.

The results for the no front and front cases are relevant to the study by Parfitt et al. (2017a), who investigated how changes to the resolution of the SST (from  $1^\circ \times 1^\circ$  grid spacing to  $0.05^\circ \times 0.05^\circ$ ) used in ERA-Interim affected the representation of atmospheric fronts in the region of the Gulf Stream. With a stronger SST front, more cold fronts were detected (using the Parfitt–Czaja–Seo method) over the Gulf Stream SST front, whereas fewer cold fronts were detected on either side of it. A similar result was found in an earlier study by Parfitt et al. (2016), who investigated how the strength of the SST front affected fronts in a general circulation model (again using the Parfitt–Czaja–Seo method). The results from Parfitt et al. (2016, 2017a) are consistent with stronger diabatic frontogenesis as the atmospheric front crosses the stronger SST front, with stronger diabatic frontolysis upstream and downstream. As shown in section 2, however, the diabatic frontogenesis is small in comparison to the adiabatic frontogenesis, and according to the one-dimensional model, there is little net frontogenesis. These results are consistent with idea that the maximum in the number of fronts detected along the SST front in ERA-Interim is due to local diabatic frontogenesis (or a weakening of the broader-scale frontolysis) in concert with adiabatic frontogenesis in initially non-frontal airstreams.

d. Implications for vertical motion and rainfall

The present work does not address the vertical circulation associated with fronts or weaker nonfrontal potential temperature gradients. Consequently, the theory developed here is unable to answer questions concerning the effect of frontogenesis on the vertical motion and rainfall. Nonetheless, previous frontal theories hint at these effects. These theories show that the vertical motion is related to the rate of frontogenesis (e.g.,

←  
(magenta), and frontogenesis  $D|\partial\theta/\partial y|/Dt$  (green). Adiabatic frontogenesis  $F_{ad} = \alpha|\partial\theta/\partial y|^{-1}\partial\theta/\partial y$  (dashed blue lines) and diabatic frontogenesis  $F_{di} = \mu|\partial\theta/\partial y|^{-1}(\partial\theta/\partial y - \partial T_S/\partial y)$  (dotted blue lines).

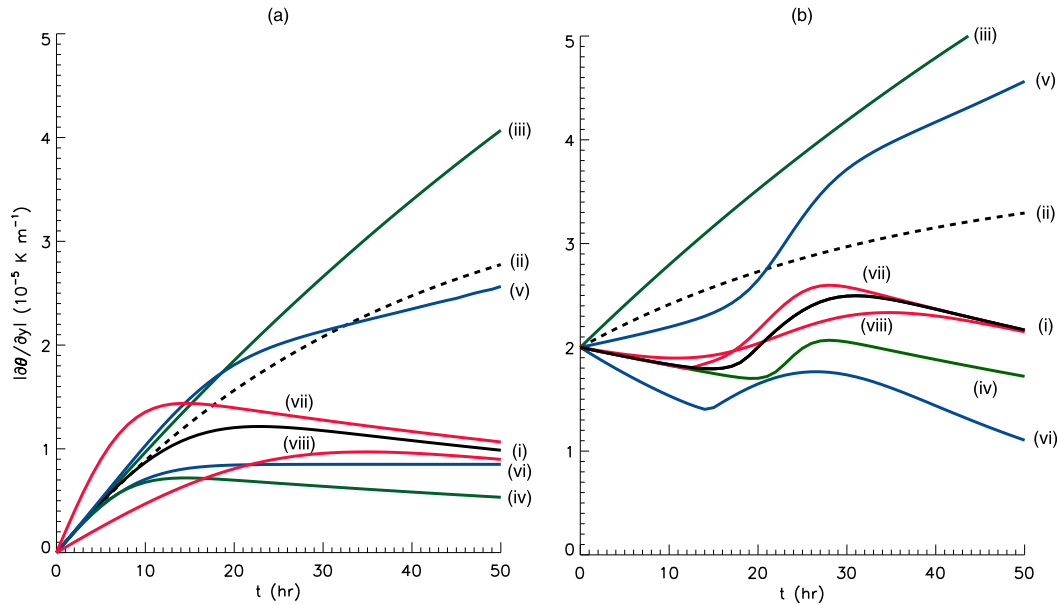


FIG. 9. Time series of the magnitude of the maximum potential temperature gradient  $|\partial\theta/\partial y|$  from the one-dimensional model. (a) No front case. (b) Front case. Control solution: Standard deformation ( $\alpha = 0.5 \times 10^{-5} \text{ s}^{-1}$ ), standard translation ( $c = 5 \text{ m s}^{-1}$ ), and standard SST gradient ( $h = 200 \text{ km}$ ) (i, black solid line). No deformation, no translation (ii, black dashed line). No translation and double the standard translation speed, respectively (iii and iv, green lines). Double the standard deformation and no deformation, respectively (v and vi, blue lines). Half and double the standard SST gradient, respectively (vii and viii, red lines).

Sawyer 1956; Eliassen 1959, 1962; Hoskins and Bretherton 1972; Keyser et al. 1988). Thus, although the simple model developed here predicts that the strength of the SST front does not determine the long-term strength of an atmospheric front or a weaker nonfrontal potential temperature gradient (unless it is stationary), the SST front can strongly affect the instantaneous rate of frontogenesis, and hence, presumably, the vertical motion and rain. Moreover, the diabatic contribution to the frontogenesis is more important in nonfrontal airstreams than for fronts [Eq. (5)], and hence the effect on rainfall may be relatively greater in nonfrontal airstreams. Of course, the validity of these inferences requires further investigation.

**4. Two-dimensional circularly symmetric vortex model of frontogenesis**

This section extends the results of the previous section to a more realistic geometry and partially accounts for the differences in the surface sensible heat flux on the warm and cold sides of the SST front. A kinematic model of frontogenesis with a two-dimensional vortex, representative of an extratropical cyclone, is derived and the interaction of the attendant cold front with an SST front is illustrated with one example.

*a. Model formulation and solution*

A steady circularly symmetric vortex  $v(r)$  is discussed now, where  $v$  is the azimuthal component of the velocity and  $r$  is the radial coordinate. The radial component of velocity is  $u = 0$  and the azimuthal coordinate is  $\lambda$ . Suppose the vortex advects the potential temperature field  $\theta(r, \lambda, t)$  while surface

fluxes proportional to the difference between the potential temperature and the sea surface temperature  $T_S(r, \lambda, t)$  modify it. Then the evolution of the potential temperature is governed by

$$\frac{D\theta}{Dt} = \frac{\partial\theta}{\partial t} + \frac{v}{r} \frac{\partial\theta}{\partial\lambda} = \mu(T_S - \theta). \tag{11}$$

The characteristics of Eq. (11) are defined by  $u = dr/dt = 0$  and  $v = (1/r)d\lambda/dt$ , which upon integrating gives  $r = r_i$  and  $\lambda(t) = \lambda_i + \Omega t$ , where  $\Omega(r) = rv$ , and  $r_i$  and  $\lambda_i$  are the values of  $r$  and  $\lambda$  at the initial time. When  $\mu$  is a constant, Eq. (11) can be solved along the characteristic curves to give

$$\theta(r, \lambda, t) = \theta_i(r, \lambda - \Omega t) e^{-\mu t} + \mu e^{-\mu t} \int_0^t e^{\mu\tau} T_S[r, \lambda - \Omega(t - \tau)] d\tau, \tag{12}$$

TABLE 1. Constants for each solution from the one-dimensional model. For the no front cases,  $\Delta\theta = 0 \text{ K}$ , whereas for the front cases,  $\Delta\theta = 20 \text{ K}$ .

	$\alpha \text{ (} 10^{-5} \text{ s}^{-1}\text{)}$	$c \text{ (m s}^{-1}\text{)}$	$h \text{ (km)}$
i (Control)	0.5	10	200
ii	0	0	200
iii	0.5	0	200
iv	0.5	20	200
v	1	10	200
vi	0	10	200
vii	0.5	10	100
viii	0.5	10	400

where  $\theta_i$  is the initial potential temperature field. In the special case when  $\mu = 0$ , there is no coupling between the sea surface and the overlying atmosphere, whereupon the vortex advects the potential temperature conservatively and the general solution reduces to  $\theta(r, \lambda, t) = \theta_i(r, \lambda - \Omega t)$ .

The near surface atmosphere is more stable when relatively warm air lies over a relatively cold sea surface than vice versa. Consequently, the surface sensible heat flux is generally smaller on the cold side of the SST front than on the warm side. In this case,  $\mu$  is not constant, and solutions can be found numerically by integrating Eq. (11) along the characteristic curves. Calculations of this kind are presented here, although the essential results are unchanged whether or not  $\mu$  is allowed to vary. Specifically,  $\mu = 7.5 \times 10^{-6} \text{ s}^{-1}$  as in the one-dimensional model when  $T_S - \theta > 0$ , and for simplicity  $\mu = 0 \text{ s}^{-1}$  otherwise. Thus, the surface sensible heating is assumed to be large and positive when cold air overlies a warm sea surface, and zero when warm air overlies a cold sea surface.

Following Keyser et al. (1988), the vortex is defined by the streamfunction  $\psi(r)$

$$\psi(r) = -\frac{\psi_0}{2} \text{sech}^2\left(\frac{r}{R}\right),$$

where  $\psi_0$  and  $R$  are constants. Then the azimuthal velocity is  $\partial\psi/\partial r$ , which is

$$v(r) = \Omega(r)r = \frac{\psi_0}{R} \text{sech}^2\left(\frac{r}{R}\right) \tanh\left(\frac{r}{R}\right).$$

Likewise, the potential temperature at the initial time is defined by

$$\theta(r, \lambda, 0) = \theta_i(r_i, \lambda_i) = \theta_0 - \frac{\Delta\theta}{2} \tanh\left[\frac{r_i \sin(\lambda_i)}{d}\right], \quad (13)$$

where  $\theta_0$ ,  $\Delta\theta$ , and  $d$  are constants. Physically, Eq. (13) represents a straight baroclinic zone oriented parallel to the  $x$  axis. Finally, the sea surface temperature is defined as

$$T_S(r, \lambda, t) = T_0 - \frac{\Delta T}{2} \tanh \times \left[ \frac{-r \cos(\lambda) \sin(\gamma) + (r \sin(\lambda) - y_0) \cos(\gamma) - ct}{h} \right], \quad (14)$$

where  $T_0$ ,  $\Delta T$ ,  $\gamma$ ,  $y_0$ ,  $c$ , and  $h$  are constants. Physically, Eq. (14) represents a straight sea surface temperature front oriented at an angle  $\gamma$  and translating with speed  $c$ .

For reference, the solution to Eq. (12) with constant  $\mu$  is

$$\begin{aligned} \theta(r, \lambda, t) = & T_0 + (\theta_0 - T_0)e^{-\mu t} - \frac{\Delta\theta}{2} e^{-\mu t} \tanh\left[\frac{r \sin(\lambda - \Omega t)}{d}\right] + \frac{\Delta T}{2} \mu e^{-\mu t} \\ & \times \int_0^t e^{\mu\tau} \tanh\left(\frac{-r \cos[\lambda - \Omega(t - \tau)] \sin(\gamma) + \{r \sin[\lambda - \Omega(t - \tau)] - y_0\} \cos(\gamma) - c\tau}{h}\right) d\tau. \end{aligned}$$

**b. Results**

The chosen constants for the numerical solution to Eq. (11) are  $\psi_0 = 2.5 \times 10^6 \text{ m}^2 \text{ s}^{-1}$ ,  $R = 500 \text{ km}$ ,  $\theta_0 = 280 \text{ K}$ ,  $\Delta\theta = 280 \text{ K}$ ,  $d = 500 \text{ km}$ ,  $T_0 = 280 \text{ K}$ ,  $\Delta T = 15 \text{ K}$ ,  $h = 200 \text{ km}$ ,  $\gamma = -\pi/12$ ,  $y_0 = -1500 \text{ km}$ , and  $c = 2.5 \text{ m s}^{-1}$ . The resulting maximum values of the vorticity and deformation associated with the streamfunction field are  $2 \times 10^{-5}$  and  $0.65 \times 10^{-5} \text{ s}^{-1}$ , respectively, and these maxima are located at  $0.66R$  and  $0.87R$ , respectively. The deformation is thus comparable to the control solutions in section 3. The values for  $\psi_0$  and  $R$  come from Keyser et al. (1988) and are consistent with the Rossby number for the vortex being small. The remaining constant are typical values derived from ERA-Interim for Northern Hemisphere winter.

Physically, the solution represents a slow-moving vortex advancing toward higher SSTs, interacting with an SST front inclined at angle  $-12^\circ$  to the  $x$  axis (Fig. 10a). At the initial time the isentropes are aligned along the  $x$  axis, but as time progresses the vortex advects the isentropes, producing a cold front to the southwest and a warm front to the northeast at 96 h (Fig. 10b). These fronts strengthen through the adiabatic frontogenesis due to the deformation associated with the vortex. Diabatic frontogenesis is negligible at 96 h, because almost everywhere  $\theta > T_S$  (green line marks  $T_S = \theta$ ). The only exception is a very thin strip on the warm side of the SST front.

By 144 h, the fronts wrap part way around the vortex, producing a structure reminiscent of bent-back warm and cold fronts separated by a frontal fracture (Fig. 10c). Adiabatic frontogenesis continues to strengthen both fronts symmetrically and is largely independent of the SST front. As the vortex and front is slow moving, there is pronounced diabatic frontogenesis where  $\theta > T_S$  (Fig. 10d), which is positive along the SST front and negative on the warm side of it. These results are consistent with the analysis presented in section 2 and with the one-dimensional model, which predicts diabatic frontogenesis as the atmospheric front crosses the front, together with diabatic frontolysis downstream.

The main point of the two-dimensional circularly symmetric vortex model of frontogenesis is to show that the results from the one-dimensional model carry over to a more realistic geometry that includes a representation of an extratropical cyclone and its attendant warm and cold fronts, and to a more realistic representation of the difference in the sensible heating on each side of the SST front.

**5. Conclusions**

The effects of SST gradients on atmospheric fronts have been investigated through a combination of observation and theory. The investigation began with a climatology of fronts and frontogenesis over the North Atlantic Ocean based on ERA-Interim. The climatologies were conditioned on whether

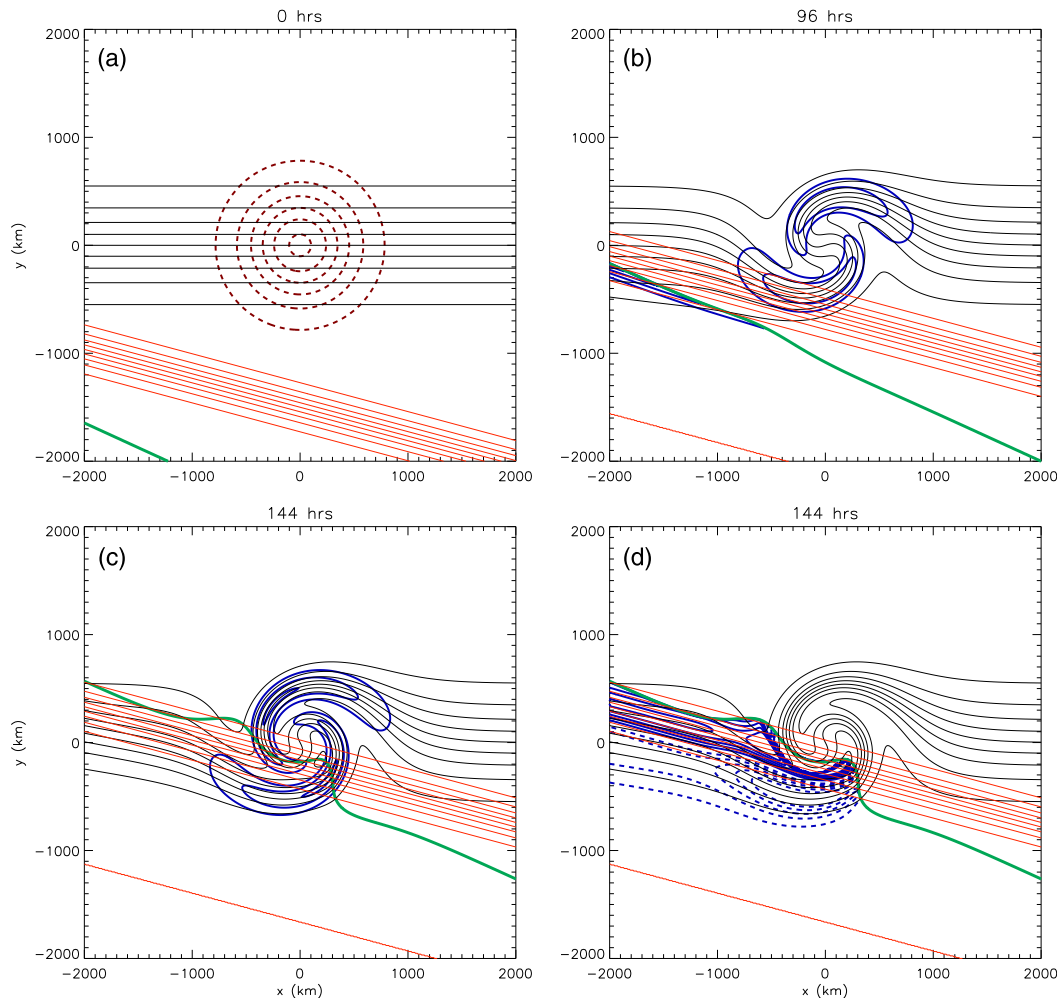


FIG. 10. Two-dimensional circular vortex model solution with  $\gamma = -\pi/12$ ,  $y_0 = -1500$  km, and  $c = 2.5$  m s<sup>-1</sup>. Potential temperature  $\theta$  (black, contour interval: 2 K), sea surface temperature  $T_S$  (red, contour interval: 2 K) and  $\theta - T_S = 0$  (green). (a) 0 h. Streamfunction  $\psi$  (brown, contour interval:  $2 \times 10^5$  m<sup>2</sup> s<sup>-1</sup>, dashed lines negative). (b) 96 h. Frontogenesis function  $D|\nabla\theta|/Dt$  (blue). (c) 144 h. Adiabatic frontogenesis function  $F_{ad}$  (blue). (d) 144 h. Diabatic frontogenesis function  $F_{di}$  (blue). (b)–(d) Contour interval:  $4 \times 10^{-11}$  K (m s)<sup>-1</sup>, with dashed lines negative and zero contour suppressed.

or not a front was detected at a point. None of the results were sensitive to the definition of a front.

The climatological mean potential temperature gradient was divided into parts attributable to times when fronts were detected at a point and times when they were not. The part attributable to the times with fronts is more focused on the SST front but weaker than that attributable to times without fronts. Thus, times without fronts contribute the greater part of the climatological low-level baroclinicity in the neighborhood of the SST front.

When a front is detected at a point, adiabatic frontogenesis is far more important than diabatic frontogenesis. This is a result foreshadowed by consideration of the ratio of the adiabatic to diabatic terms in the frontogenesis function, which is directly proportional to the magnitude of the potential temperature gradient and inversely proportional to the magnitude of the diabatic heating gradient across the baroclinic zone. Moreover,

the adiabatic frontogenesis is mainly due to deformation as the contribution from convergence is nearly an order of magnitude smaller. The pattern of adiabatic frontogenesis has a broad maximum in the western North Atlantic associated with the regular occurrence of cyclones along the storm track, whereas the diabatic frontogenesis is weakly positive over the SST front and negative on either side.

When a front is not detected at a point, the adiabatic frontogenesis (which is again mainly due to deformation) is weaker and broader than when a front is detected. The diabatic frontogenesis is, however, relatively strong along the SST front, with comparable frontolysis on the equatorward side. Differential surface sensible heating affects atmospheric fronts directly through the diabatic frontogenesis and indirectly through the adiabatic frontogenesis as the deformation amplifies the direct effect. This combination of adiabatic



frontogenesis and strong localized diabatic frontogenesis occasionally culminates in the detection of a front, which is consistent with atmospheric fronts being most frequently located (around 15% of the time) along the SST front.

The climatologies motivated two highly simplified kinematic models of the effects of SST gradients on atmospheric frontogenesis, both of which were extensions of those developed by Keyser et al. (1988). The first model was a one-dimensional model of frontogenesis. It was based on a wind field with hyperbolic streamlines (sometimes called a confluent deformation model), and described the passage of an air mass over an SST front. The calculations assumed one of two specific initial conditions: the case in which there was no potential temperature gradient, called the no front case, and the case in which there was a 20 K difference in potential temperature within the air mass, called the front case. The second model of frontogenesis described a two-dimensional vortex, representative of an extratropical cyclone, and its associated fronts, interacting with an SST front. The main purpose of the two-dimensional model was to demonstrate that the results of the one-dimensional model were unchanged in a geometrically more realistic setting and when differences in the sensible heating on each side of the SST front were taken into account.

There are many omissions from both models, but the main ones were the lack of a boundary layer and the associated turbulent dissipation, a simplified treatment of the surface sensible heat fluxes, and the lack of moist processes. Despite these omissions, both models proved to have a great deal of explanatory power, suggesting the main dynamical and diabatic processes had been retained.

In the front case, there is a period of relatively weak frontogenesis as the model front crosses the SST front, but because of the upstream and downstream frontolysis, the SST front is unimportant in determining the *long-term* strength of the atmospheric front. Importantly, this result changes little in the model as the width of the SST gradient changes. In line with the climatology, the long-term strength of the potential temperature gradient characterizing the atmospheric front is largely determined by the deformation. If the deformation is sufficiently strong, the diabatic frontogenesis overwhelms the frontolytic effects of diabatic frontogenesis on either side of the SST front. In the no front cases, there is sustained frontogenesis in the model only when the deformation is sufficiently strong or when the translation speed is low, as advection otherwise weakens the potential temperature gradient. As the cold air mass crosses the SST front, the model produces strong diabatic frontogenesis followed by frontolysis. This result agrees with the climatologies for the North Atlantic, where the dominant contribution to the climatological diabatic frontogenesis along the SST comes from the no front cases.

The simple models explain why more fronts are detected along the SST front than either side of it. Strong diabatic frontolysis decreases equivalent potential temperature gradients either side of the SST front, while the combination of diabatic frontogenesis (or weaker diabatic frontolysis) and diabatic frontogenesis increases equivalent potential temperature gradients along the SST front. Consequently, an equivalent potential temperature gradient is more likely to

exceed the detection threshold for a front over the SST front than either side of it.

*Acknowledgments.* We are grateful to three anonymous reviewers, who helped significantly improve the paper. We also acknowledge the indispensable contribution from the ECMWF though their provision of ERA-Interim. MJR was supported by the Research Council of Norway project UNPACC (262220) and the Australian Research Council Centre of Excellence for Climate Extremes (CE170100023).

*Data availability statement.* The data used to construct the climatologies are from the ERA-Interim and are available at <https://apps.ecmwf.int/datasets/>.

## REFERENCES

- Bergeron, T., 1928: Über die dreidimensional verknüpfende Wetteranalyse I. *Geophys. Publ.*, **5**, 1–11.
- Berry, G., M. J. Reeder, and C. Jakob, 2011: A global climatology of atmospheric fronts. *Geophys. Res. Lett.*, **38**, L04809, <https://doi.org/10.1029/2010GL046451>.
- Bui, H., and T. Spengler, 2021: On the influence of sea surface temperature distributions on the development of extratropical cyclones. *J. Atmos. Sci.*, **78**, 1173–1188, <https://doi.org/10.1175/JAS-D-20-0137.1>.
- Chang, E. K. M., S. Lee, and K. L. Swanson, 2002: Storm track dynamics. *J. Climate*, **15**, 2163–2183, [https://doi.org/10.1175/1520-0442\(2002\)015<0216:STD>2.0.CO;2](https://doi.org/10.1175/1520-0442(2002)015<0216:STD>2.0.CO;2).
- Dee, D. P., and Coauthors, 2011: The ERA-Interim reanalysis: Configuration and performance of the data assimilation system. *Quart. J. Roy. Meteor. Soc.*, **137**, 553–587, <https://doi.org/10.1002/qj.828>.
- de Vries, H., S. Scher, R. Haarsma, S. Drijfhout, and A. van Delden, 2019: How Gulf-Stream SST-fronts influence Atlantic winter storms. *Climate Dyn.*, **52**, 5899–5909, <https://doi.org/10.1007/s00382-018-4486-7>.
- Eliassen, A., 1959: On the formation of fronts in the atmosphere. *The Atmosphere and Sea in Motion*, Rockefeller Institute Press, 277–287.
- , 1962: On the vertical circulation in frontal zones. *Geophys. Publ.*, **24**, 147–160.
- Gyakum, J. R., J. R. Anderson, R. H. Grumm, and E. L. Gruner, 1989: North Pacific cold-season surface cyclone activity: 1975–1983. *Mon. Wea. Rev.*, **117**, 1141–1155, [https://doi.org/10.1175/1520-0493\(1989\)117<1141:NPCCSS>2.0.CO;2](https://doi.org/10.1175/1520-0493(1989)117<1141:NPCCSS>2.0.CO;2).
- Hoskins, B. J., and F. P. Bretherton, 1972: Atmospheric frontogenesis models: Mathematical formulation and solution. *J. Atmos. Sci.*, **29**, 11–37, [https://doi.org/10.1175/1520-0469\(1972\)029<0011:AFMMFA>2.0.CO;2](https://doi.org/10.1175/1520-0469(1972)029<0011:AFMMFA>2.0.CO;2).
- , and P. J. Valdes, 1990: On the existence of storm tracks. *J. Atmos. Sci.*, **47**, 1854–1864, [https://doi.org/10.1175/1520-0469\(1990\)047<1854:OTEOST>2.0.CO;2](https://doi.org/10.1175/1520-0469(1990)047<1854:OTEOST>2.0.CO;2).
- Hotta, D., and H. Nakamura, 2011: On the significance of sensible heat supply from the ocean in the maintenance of mean baroclinicity along storm tracks. *J. Climate*, **24**, 3377–3401, <https://doi.org/10.1175/2010JCLI3910.1>.
- Jacobs, N. A., S. Raman, G. M. Lackmann, and P. P. Childs, 2008: The influence of the Gulf Stream induced SST gradients on the US East Coast winter storm of 24–25 January 2000. *Int. J. Remote Sens.*, **29**, 6145–6174, <https://doi.org/10.1080/0143160802175561>.

- Kelly, K. A., R. J. Small, R. M. Samelson, B. Qiu, T. M. Joyce, Y.-O. Kwon, and M. F. Cronin, 2010: Western boundary currents and frontal air–sea interaction: Gulf Stream and Kuroshio Extension. *J. Climate*, **23**, 5644–5667, <https://doi.org/10.1175/2010JCLI3346.1>.
- Keyser, D., M. J. Reeder, and R. J. Reed, 1988: A generalization of Pettersen's frontogenesis function and its relation to the forcing of vertical motion. *Mon. Wea. Rev.*, **116**, 762–781, [https://doi.org/10.1175/1520-0493\(1988\)116<0762:AGOPFF>2.0.CO;2](https://doi.org/10.1175/1520-0493(1988)116<0762:AGOPFF>2.0.CO;2).
- Masunaga, R., H. Nakamura, B. Taguchi, and T. Miyasaka, 2020a: Processes shaping the frontal-scale time-mean surface wind convergence patterns around the Gulf Stream and Agulhas Return Current in winter. *J. Climate*, **33**, 9083–9101, <https://doi.org/10.1175/JCLI-D-19-0948.1>.
- , —, —, and —, 2020b: Processes shaping the frontal-scale time-mean surface wind convergence patterns around the Kuroshio Extension in winter. *J. Climate*, **33**, 3–25, <https://doi.org/10.1175/JCLI-D-19-0097.1>.
- Minobe, S., A. Kuwano-Yoshida, N. Komori, S.-P. Xie, and R. J. Small, 2008: Influence of the Gulf Stream on the troposphere. *Nature*, **452**, 206–209, <https://doi.org/10.1038/nature06690>.
- , M. Miyashita, A. Kuwano-Yoshida, H. Tokinaga, and S.-P. Xie, 2010: Atmospheric response to the Gulf Stream: Seasonal variations. *J. Climate*, **23**, 3699–3719, <https://doi.org/10.1175/2010JCLI3359.1>.
- Nakamura, H., T. Sampe, Y. Tanimoto, and A. Shimpo, 2004: Observed associations among storm tracks, jet streams and midlatitude oceanic fronts. *Earth's Climate: The Ocean-Atmosphere Interactions*, C. Wang, S. Xie, and J. Carton, Eds., Amer. Geophys. Union, 329–345, <https://doi.org/10.1029/147GM18>.
- , —, A. Goto, W. Ohfuchi, and S.-P. Xie, 2008: On the importance of midlatitude oceanic frontal zones for the mean state and dominant variability in the tropospheric circulation. *Geophys. Res. Lett.*, **35**, L15709, <https://doi.org/10.1029/2008GL034010>.
- Ogawa, F., and T. Spengler, 2019: Prevailing surface wind direction during air–sea heat exchange. *J. Climate*, **32**, 5601–5617, <https://doi.org/10.1175/JCLI-D-18-0752.1>.
- O'Neill, L. W., T. Haack, D. B. Chelton, and E. Skillingstad, 2017: The Gulf Stream convergence zone in the time-mean winds. *J. Atmos. Sci.*, **74**, 2383–2412, <https://doi.org/10.1175/JAS-D-16-0213.1>.
- Papritz, L., and T. Spengler, 2015: Analysis of the slope of isentropic surfaces and its tendencies over the North Atlantic. *Quart. J. Roy. Meteor. Soc.*, **141**, 3226–3238, <https://doi.org/10.1002/qj.2605>.
- Parfitt, R., and H. Seo, 2018: A new framework for near-surface wind convergence over the Kuroshio Extension and Gulf Stream in wintertime: The role of atmospheric fronts. *Geophys. Res. Lett.*, **45**, 9909–9918, <https://doi.org/10.1029/2018GL080135>.
- , and Y.-O. Kwon, 2020: The modulation of Gulf Stream influence on the troposphere by the eddy-driven jet. *J. Climate*, **33**, 4109–4120, <https://doi.org/10.1175/JCLI-D-19-0294.1>.
- , A. Czaja, S. Minobe, and A. Kuwano-Yoshida, 2016: The atmospheric frontal response to SST perturbations in the Gulf Stream region. *Geophys. Res. Lett.*, **43**, 2299–2306, <https://doi.org/10.1002/2016GL067723>.
- , —, and Y.-O. Kwon, 2017a: The impact of SST resolution change in the ERA-Interim reanalysis on wintertime Gulf Stream frontal air–sea interaction. *Geophys. Res. Lett.*, **44**, 3246–3254, <https://doi.org/10.1002/2017GL073028>.
- , —, and H. Seo, 2017b: A simple diagnostic for the detection of atmospheric fronts. *Geophys. Res. Lett.*, **44**, 4351–4358, <https://doi.org/10.1002/2017GL073662>.
- Petterssen, S., 1936: Contributions to the theory of frontogenesis. *Geophys. Publ.*, **11**, 1–27.
- Putrasahan, D. A., A. J. Miller, and H. Seo, 2013: Isolating meso-scale coupled ocean-atmosphere interactions in the Kuroshio Extension region. *Dyn. Atmos. Oceans*, **63**, 60–78, <https://doi.org/10.1016/j.dynatmoce.2013.04.001>.
- Robinson, W. A., 2000: Review of WETS—The workshop on extra-tropical SST anomalies. *Bull. Amer. Meteor. Soc.*, **81**, 567–578, [https://doi.org/10.1175/1520-0477\(2000\)081<0567:ROWTWO>2.3.CO;2](https://doi.org/10.1175/1520-0477(2000)081<0567:ROWTWO>2.3.CO;2).
- Sanders, F., and J. R. Gyakum, 1980: Synoptic-dynamic climatology of the “bomb.” *Mon. Wea. Rev.*, **108**, 1589–1606, [https://doi.org/10.1175/1520-0493\(1980\)108<1589:SDCOT>2.0.CO;2](https://doi.org/10.1175/1520-0493(1980)108<1589:SDCOT>2.0.CO;2).
- Sasaki, Y. N., and Y. Yamada, 2018: Atmospheric response to interannual variability of sea surface temperature front in the East China Sea in early summer. *Climate Dyn.*, **51**, 2509–2522, <https://doi.org/10.1007/s00382-017-4025-y>.
- Saucier, W. J., 1955: *Principles of Meteorological Analysis*. University of Chicago Press, 454 pp.
- Sawyer, J. S., 1956: The vertical circulation at meteorological fronts and its relation to frontogenesis. *Proc. Roy. Soc. London.*, **234A**, 346–362, <https://doi.org/10.1098/RSPA.1956.0039>.
- Sheldon, L., and Coauthors, 2017: A ‘warm path’ for Gulf Stream troposphere interactions. *Tellus*, **69A**, 1299397, <https://doi.org/10.1080/16000870.2017.1299397>.
- Small, R. J., R. Msadek, Y.-O. Kwon, J. F. Booth, and C. Zarzycki, 2019: Atmosphere surface storm track response to resolved ocean mesoscale in two sets of global climate model experiments. *Climate Dyn.*, **52**, 2067–2089, <https://doi.org/10.1007/s00382-018-4237-9>.
- Smith, R. K., and M. J. Reeder, 1988: On the movement and low-level structure of cold fronts. *Mon. Wea. Rev.*, **116**, 1927–1944, [https://doi.org/10.1175/1520-0493\(1988\)116<1927:OTMALL>2.0.CO;2](https://doi.org/10.1175/1520-0493(1988)116<1927:OTMALL>2.0.CO;2).
- Solman, S. A., and I. Orlanski, 2010: Subpolar high anomaly preconditioning precipitation over South America. *J. Atmos. Sci.*, **67**, 1526–1542, <https://doi.org/10.1175/2009JAS3309.1>.
- Spensberger, C., and M. Sprenger, 2018: Beyond cold and warm: An objective classification for maritime midlatitude fronts. *Quart. J. Roy. Meteor. Soc.*, **144**, 261–277, <https://doi.org/10.1002/qj.3199>.
- Stone, P. H., 1966: Frontogenesis by horizontal wind deformation fields. *J. Atmos. Sci.*, **23**, 455–465, [https://doi.org/10.1175/1520-0469\(1966\)023<0455:FBHWF>2.0.CO;2](https://doi.org/10.1175/1520-0469(1966)023<0455:FBHWF>2.0.CO;2).
- Thomas, C. M., and D. M. Schultz, 2019: What are the best thermodynamic quantity and function to define a front in gridded model output? *Bull. Amer. Meteor. Soc.*, **100**, 873–895, <https://doi.org/10.1175/BAMS-D-18-0137.1>.
- Tsopouridis, L., T. Spengler, and C. Spensberger, 2020: SST fronts along the Gulf Stream and Kuroshio affect the winter climatology primarily in the absence of cyclones. *Wea. Climate Dyn. Discuss.*, <https://doi.org/10.5194/wcd-2020-50>.
- , C. Spensberger, and T. Spengler, 2021a: Characteristics of cyclones following different pathways in the Gulf Stream region. *Quart. J. Roy. Meteor. Soc.*, **147**, 392–407, <https://doi.org/10.1002/qj.3924>.
- , —, and —, 2021b: Cyclone intensification in the Kuroshio region and its relation to the sea surface temperature front and

- upper-level forcing. *Quart. J. Roy. Meteor. Soc.*, **147**, 485–500, <https://doi.org/10.1002/qj.3929>.
- Vannière, B., A. Czaja, H. F. Dacre, and T. Woollings, 2017: A “cold path” for the Gulf Stream–troposphere connection. *J. Climate*, **30**, 1363–1379, <https://doi.org/10.1175/JCLI-D-15-0749.1>.
- Williams, R. T., 1967: Atmospheric frontogenesis: A numerical experiment. *J. Atmos. Sci.*, **24**, 627–641, [https://doi.org/10.1175/1520-0469\(1967\)024<0627:AFANE>2.0.CO;2](https://doi.org/10.1175/1520-0469(1967)024<0627:AFANE>2.0.CO;2).
- , and J. Plotkin, 1968: Quasi-geostrophic frontogenesis. *J. Atmos. Sci.*, **25**, 201–206, [https://doi.org/10.1175/1520-0469\(1968\)025<0201:QGF>2.0.CO;2](https://doi.org/10.1175/1520-0469(1968)025<0201:QGF>2.0.CO;2).
- Yoshiike, S., and R. Kawamura, 2009: Influence of wintertime large-scale circulation on the explosively developing cyclones over the western North Pacific and their downstream effects. *J. Geophys. Res.*, **114**, D13110, <https://doi.org/10.1029/2009JD011820>.